

PCSK9 drives sterol-dependent metastatic organ choice in pancreatic cancer

<https://doi.org/10.1038/s41586-025-09017-8>

Received: 2 June 2024

Accepted: 14 April 2025

Published online: 21 May 2025

 Check for updates

Gilles Rademaker^{1,2}, Grace A. Hernandez^{1,2}, Yurim Seo³, Sumena Dahal^{1,2}, Lisa Miller-Phillips^{2,4}, Alexander L. Li¹, Xianlu Laura Peng⁵, Changfei Luan⁵, Longhui Qiu³, Maude A. Liegeois⁶, Bruce Wang^{2,7}, Kwun W. Wen⁸, Grace E. Kim⁹, Eric A. Collisson⁹, Stephan F. Kruger⁴, Stefan Boeck^{4,10,11}, Steffen Ormanns^{12,13}, Michael Guenther^{12,13}, Volker Heinemann⁴, Michael Haas^{4,10}, Mark R. Looney³, Jen Jen Yeh^{5,14}, Roberto Zoncu¹⁵ & Rushika M. Perera^{1,2,8}✉

To grow at distant sites, metastatic cells must overcome major challenges posed by the unique cellular and metabolic composition of secondary organs¹. Pancreatic ductal adenocarcinoma (PDAC) is an aggressive disease that metastasizes to the liver and lungs. Despite evidence of metabolic reprogramming away from the primary site, the key drivers that dictate the ability of PDAC cells to colonize the liver or lungs and survive there remain undefined. Here we identified PCSK9 as predictive of liver versus lung colonization by integrating metastatic tropism data of human PDAC cell lines², *in vivo* metastasis modelling in mice and gene expression correlation analysis. PCSK9 negatively regulates low density lipoprotein (LDL)-cholesterol import and, accordingly, PCSK9-low PDAC cells preferentially colonize LDL-rich liver tissue. LDL-cholesterol taken up by liver-avid PCSK9-low cells supports activation of pro-growth mTORC1 activation at the lysosome, and through conversion into the signalling oxysterol, 24(S)-hydroxycholesterol, reprogrammes the microenvironment to release nutrients from neighbouring hepatocytes. Conversely, PCSK9-high, lung-avid PDAC cells rely on transcriptional upregulation of the distal cholesterol synthesis pathway to generate intermediates—7-dehydrocholesterol and 7-dehydrodesmosterol—with protective action against ferroptosis, a vulnerability in the oxygen-rich microenvironment of the lung. Increasing the amount of PCSK9 redirected liver-avid cells to the lung whereas ablating PCSK9 drove lung-avid cells to the liver, thereby establishing PCSK9 as necessary and sufficient for secondary organ site preference. Our studies reveal PCSK9-driven differential utilization of the distal cholesterol synthesis pathway as a key and potentially actionable driver of metastatic growth in PDAC.

Metastatic colonization requires tumour cells to adapt to microenvironments that differ from their primary site³. The mechanisms that enable outgrowth in secondary organs with distinct nutrient, cellular and structural characteristics remain poorly understood. Metabolic plasticity of tumour cells is key to survival in circulation and adaptation to new niches¹. Similarly, the metabolic profile of the target organ imposes selective pressure, allowing only suitably adapted cells to thrive⁴. PDAC frequently metastasizes to the liver, lungs, peritoneum and lymph nodes⁵; however, the specific target organ has relevance for disease progression, with lung-only metastases being linked to better outcomes than liver or multi-site spread^{6–9}. Although several

pathways have been associated with PDAC metastasis^{10–16}, the determinants of organ preference and niche-specific growth remain unclear. Here we show that PCSK9 regulates the availability of specific cholesterol intermediates and derivatives, which help tumour cells overcome organ-specific challenges associated with growth in the liver and lung.

Differential organ preference of PDAC cells

High-throughput pooled *in vivo* screens using barcoded human cancer cell lines² have revealed organ-specific metastasis patterns across tumour types, including PDAC, which frequently spreads to the liver

¹Department of Anatomy, University of California San Francisco, San Francisco, CA, USA. ²Helen Diller Family Comprehensive Cancer Center, University of California, San Francisco, CA, USA.

³Department of Medicine, University of California San Francisco, San Francisco, CA, USA. ⁴Department of Hematology/Oncology, LMU Klinikum, University of Munich Comprehensive Cancer Center, Munich, Germany. ⁵Department of Pharmacology, Lineberger Comprehensive Cancer Center, University of North Carolina at Chapel Hill, Chapel Hill, NC, USA. ⁶Cardiovascular Research Institute, University of California San Francisco, San Francisco, CA, USA. ⁷Division of Gastroenterology, Department of Medicine, University of California, San Francisco, San Francisco, CA, USA.

⁸Department of Pathology, University of California San Francisco, San Francisco, CA, USA. ⁹Fred Hutchinson Cancer Research Center, Seattle, WA, USA. ¹⁰Department of Hematology and Oncology, München Klinik Neuperlach, Munich, Germany. ¹¹German Cancer Consortium (DKTK), Munich, Germany. ¹²Institute of General Pathology, Medical University Innsbruck, Innsbruck, Austria. ¹³Innpath Institute for Pathology, Tirol Kliniken, Innsbruck, Austria. ¹⁴Departments of Surgery and Pharmacology, University of North Carolina at Chapel Hill, Chapel Hill, NC, USA.

¹⁵Department of Molecular and Cell Biology, University of California Berkeley, Berkeley, CA, USA. ✉e-mail: rushika.perera@ucsf.edu

Article

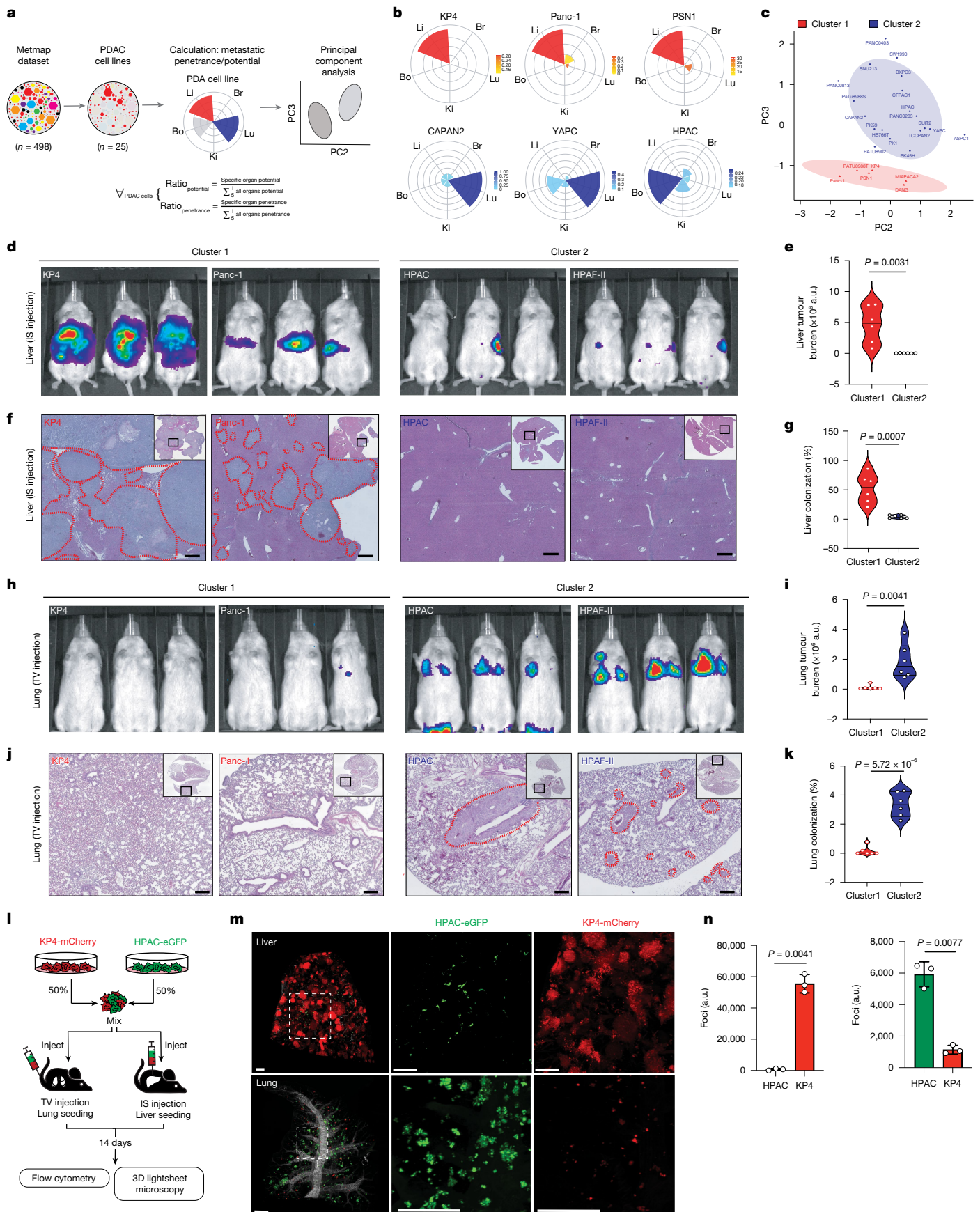


Fig. 1 | See next page for caption.

Fig. 1 | Differential organ preference of PDAC cells. **a**, Workflow for deriving metastatic potential and penetrance of PDAC cell lines using the MetMap500 database. **b**, Petal plots depicting metastatic potential (length) and penetrance (colour) for the indicated cell lines. Br, brain; Bo, bone; Ki, kidney; Li, liver; Lu, lung. **c**, Scatter plot representing two principal components derived from principal component analysis of PDAC metastatic potential and penetrance data. Each point represents an individual PDAC cell line. Two clusters are depicted. **d,e**, Normalized bioluminescence imaging (**d**) and quantification (**e**) of mice following intrasplenic (IS) injection of the indicated cluster 1 or cluster 2 cell lines stably expressing luciferase ($n = 3$ mice per cell line). a.u., arbitrary units. **f,g**, Representative haematoxylin and eosin (H&E) images showing tumour invasion in the liver with lesions outlined in red (**f**) and quantification of per cent tumour area (**g**). $n = 6$ images per group. Scale bars, 500 μ m.

h,i, Normalized bioluminescence imaging (**h**) and quantification (**i**) of mice following tail vein (TV) injection of the indicated cluster 1 and cluster 2 cell lines stably expressing luciferase ($n = 3$ mice per cell line). **j,k**, Representative H&E images showing tumour invasion in the lungs, with lesions outlined in red (**j**) and quantification of per cent tumour area (**k**). $n = 6$ images per group. Scale bars, 500 μ m. **l**, Schematic depicting experimental design for the *in vivo* cell seeding experiments. **m**, Representative light-sheet microscopy images of whole liver (top) and lung (bottom) two weeks post-injection, showing aSMA (white), HPAC-eGFP cells (green) and KP4-mCherry cells (red). Regions of interest are indicated by dotted lines. Scale bars, 1 mm. **n**, Quantification of eGFP (HPAC) and mCherry (KP4) foci from liver lobes (left; $n = 3$ mice) and lung lobes (right; $n = 3$ mice). Error bars depict s.d. Statistical significance was calculated using a two-tailed *t*-test (**e,g,i,k,n**).

and lungs. Using data from these screens (<https://depmap.org/metmap/>), we calculated fractional seeding ratios for 25 PDAC cell lines across 5 metastatic sites (liver, lung, kidney, brain and bone) (Fig. 1a,b and Extended Data Fig. 1a,b). This analysis identified two PDAC subtypes: one that has a strong preference for liver colonization (cluster 1) and another that favours other organs, notably the lungs (cluster 2) (Fig. 1c). Cluster 1 exhibited a mean liver metastatic potential of 70.6% and penetrance of 37.9%, whereas cluster 2 showed low liver tropism (3.5% potential, 9.8% penetrance) and higher lung affinity (31.2% potential, 51.3% penetrance) (Extended Data Fig. 1a,b and Supplementary Table 1).

To validate the metastatic behaviour of PDAC clusters, we tested four human PDAC cell lines (KP4, Panc-1, HPAC and HPAF-II) for liver and lung colonization using intrasplenic and tail vein injections. Intrasplenic injection of KP4 or Panc-1 led to liver tumours within four weeks, whereas HPAC and HPAF-II did not grow in the liver (Fig. 1d–g). Conversely, tail vein injection resulted in lung tumours from HPAC and HPAF-II, but not from KP4 or Panc-1 (Fig. 1h–k). Introduction of each cell line into the blood stream via intracardiac injection further confirmed these patterns: KP4 and Panc-1 preferentially colonized the liver, whereas HPAC and HPAF-II favoured the lungs (Extended Data Fig. 1c,d). Notably, all four cell lines share identical KRAS, CDKN2A and TPS3 mutations, suggesting that somatic drivers do not explain organ-specific colonization. Together, these results suggest that secondary organ preference can be modelled *in vivo* using human PDAC cell lines, and we identify two subsets with avidity towards the liver (cluster 1, C1-Liver) or lungs (cluster 2, C2-Lung).

To determine whether differential colonization by C1-Liver and C2-Lung cells reflects differences in seeding or outgrowth, we co-injected equal numbers of mCherry-labelled KP4 (KP4-R, C1-Liver) and eGFP-labelled HPAC (HPAC-G, C2-Lung) cells via intrasplenic (liver) or tail vein (lung) routes (Fig. 1l). After 14 days—a time frame sufficient for seeding but not overgrowth—we analysed organs by flow cytometry and 3D light-sheet microscopy. Flow cytometry-based analysis showed enrichment for KP4-R cells in the liver, whereas HPAC-G cells dominated in the lungs (Extended Data Fig. 1e). Light-sheet microscopy showed large KP4-R foci and very few HPAC-G foci in the liver, and the reverse was observed in the lungs (Fig. 1m,n and Supplementary Videos 1 and 2). These data indicate that both cell types can reach each organ, but C1-Liver cells preferentially grow in the liver, whereas C2-Lung cells thrive in the lungs.

Organ preference correlates with PDAC subtype

Prior transcriptional profiling studies have shown that PDAC can be stratified into two main transcriptional subtypes termed ‘basal’ and ‘classical’, which are linked to distinct molecular features and patient prognosis^{17–21}. For instance, basal PDAC displays features of poor differentiation, whereas classical PDAC is well-differentiated. We find that classical gene signatures were enriched in C2-Lung lines, whereas liver avidity was negatively correlated with this subtype (Extended

Data Fig. 1f,g and Supplementary Table 2). Histological analysis of human PDAC metastases showed that most lung lesions (9 out of 10) were well-differentiated with high nuclear staining for GATA6—a transcription factor associated with the classical subtype²² (Extended Data Fig. 1h–k). By contrast, liver lesions (35 out of 45) were poorly differentiated, lacked GATA6, and showed high nuclear ZEB1 staining (Extended Data Fig. 1h–m and Supplementary Table 3), consistent with basal-like features^{20–24}. To test whether subtype determines organ avidity, we utilized CRISPR-mediated gene silencing to knock out GATA6 in HPAC cells. Although this shifted transcriptional profiles from classical to basal (Extended Data Fig. 2a,b), GATA6 loss did not affect growth or metastatic colonization (Extended Data Fig. 2c–f). Thus, we sought to determine additional parameters, which function in parallel, that may define secondary organ site preference.

PCSK9 levels correlate with organ preference

To identify molecular features that distinguish liver-avid versus lung-avid PDAC lines, we performed gene expression correlation analysis (<https://depmap.org/>) and identified PCSK9 to be the top enriched transcript in GATA6-positive C2-Lung lines (Fig. 2a). High PCSK9 transcript and protein expression correlated with additional classical subtype markers (CDH1, S100P and FOXQ1) and was inversely correlated with basal markers (ZEB1 and VIM) (Fig. 2b and Extended Data Fig. 3a,b). PCSK9 is a serine protease that regulates cholesterol homeostasis by binding to the LDL receptor (LDLR) and promoting its lysosomal degradation, thereby suppressing LDL import (Fig. 2c). C2-Lung cells showed increased expression and secretion of PCSK9 and reduced total and cell surface levels of LDLR protein (Fig. 2b and Extended Data Fig. 3c–e). By contrast, C1-Liver lines had little or no PCSK9 and expressed high total and cell surface LDLR levels (Fig. 2b and Extended Data Fig. 3d,e). Similarly, mouse PDAC cell lines derived from a genetically engineered mouse model of PDAC (referred to as KPC²⁵), showed a similar inverse relationship between PCSK9 and LDLR (Extended Data Fig. 3f), with PCSK9-low lines colonizing the liver and PCSK9-high lines favouring the lung (Extended Data Fig. 3g,h).

To evaluate expression of PCSK9 and LDLR in primary and metastatic PDAC, we performed immunohistochemical staining of primary specimens from patients with PDAC. Poorly differentiated primary tumours and liver metastases had low expression of PCSK9 and high expression of LDLR, whereas well-differentiated tumours and lung metastases had high PCSK9 expression and low LDLR expression (Fig. 2d–g and Supplementary Tables 4 and 5). We next utilized a matched cohort of primary PDAC from patients who subsequently developed liver (liver cohort) or lung (lung cohort) only metastases²⁶ (Supplementary Table 6). PDAC tumours from the liver cohort exhibited low PCSK9 and high LDLR staining within the ductal epithelia, whereas tumours from the lung cohort showed high PCSK9 and low LDLR staining (Fig. 2h,i). Analysis of single-cell RNA-sequencing data from primary PDAC and the matched liver metastases²⁷ further confirmed PCSK9 enrichment in classical

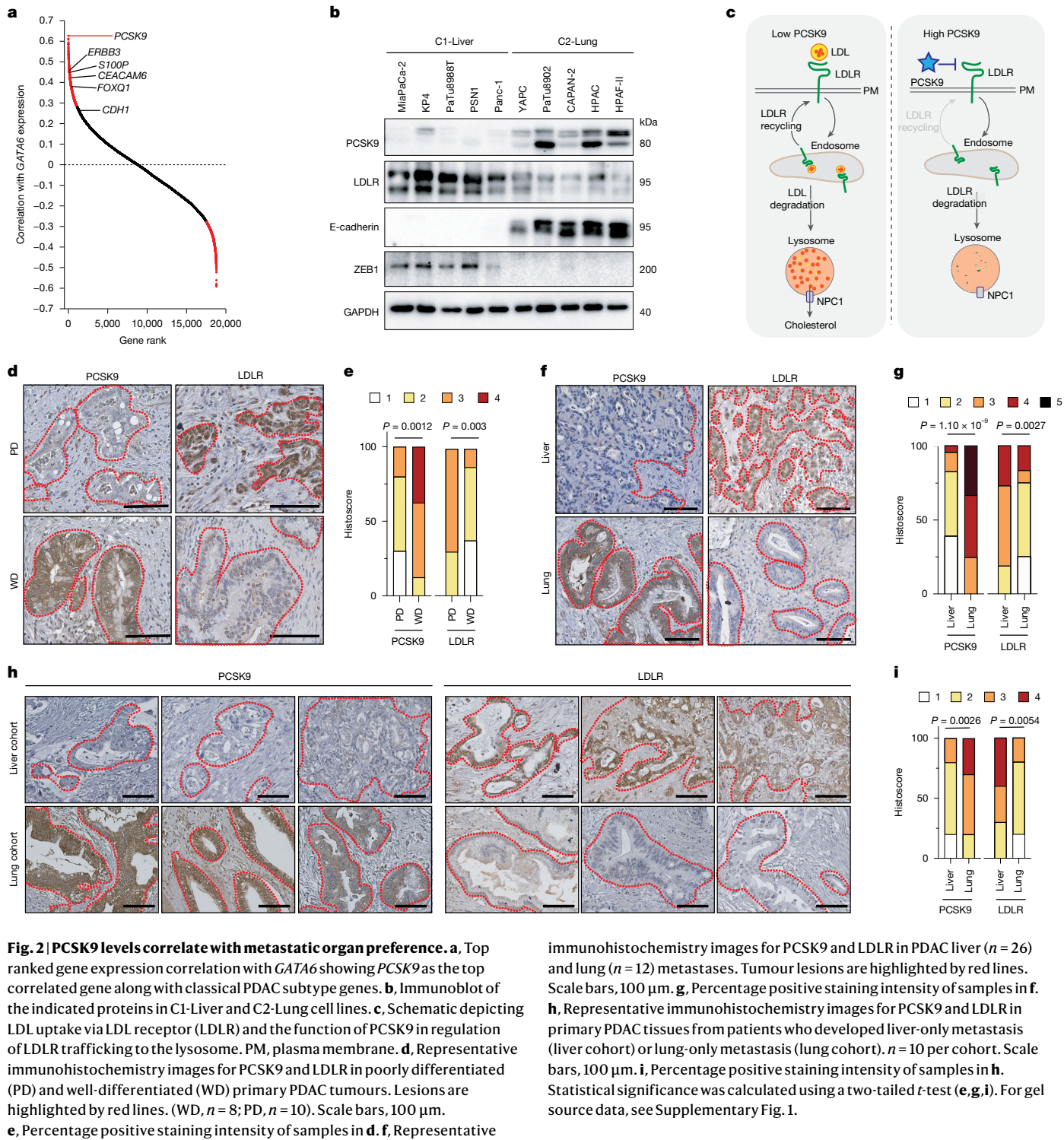


Fig. 2 | PCSK9 levels correlate with metastatic organ preference. **a**, Top ranked gene expression correlation with *GATA6* showing *PCSK9* as the top correlated gene along with classical PDAC subtype genes. **b**, Immunoblot of the indicated proteins in C1-Liver and C2-Lung cell lines. **c**, Schematic depicting LDL uptake via LDL receptor (LDLR) and the function of PCSK9 in regulation of LDLR trafficking to the lysosome. PM, plasma membrane. **d**, Representative immunohistochemistry images for PCSK9 and LDLR in poorly differentiated (PD) and well-differentiated (WD) primary PDAC tumours. Lesions are highlighted by red lines. (WD, n = 8; PD, n = 10). Scale bars, 100 μ m. **e**, Percentage positive staining intensity of samples in **d**. **f**, Representative immunohistochemistry images for PCSK9 and LDLR in primary PDAC tissues from patients who developed liver-only metastasis (liver cohort) or lung-only metastasis (lung cohort). n = 10 per cohort. Scale bars, 100 μ m. **g**, Percentage positive staining intensity of samples in **f**. Statistical significance was calculated using a two-tailed t-test (**e,g,i**). For gel source data, see Supplementary Fig. 1.

immunohistochemistry images for PCSK9 and LDLR in PDAC liver (n = 26) and lung (n = 12) metastases. Tumour lesions are highlighted by red lines. Scale bars, 100 μ m. **g**, Percentage positive staining intensity of samples in **f**. **h**, Representative immunohistochemistry images for PCSK9 and LDLR in primary PDAC tissues from patients who developed liver-only metastasis (liver cohort) or lung-only metastasis (lung cohort). n = 10 per cohort. Scale bars, 100 μ m. **i**, Percentage positive staining intensity of samples in **h**. Statistical significance was calculated using a two-tailed t-test (**e,g,i**). For gel source data, see Supplementary Fig. 1.

subtype clusters and its reduction in liver metastases compared with matched primary tumours (Extended Data Fig. 3i–m). Together these findings link low PCSK9 expression to poor differentiation and liver metastasis, and high PCSK9 expression to well-differentiated PDAC and lung metastasis.

PCSK9-low liver-avid cells uptake LDL-cholesterol

We next mechanistically evaluated the functional role of PCSK9 in linking regulation of cholesterol homeostasis to target organ selection and colonization. C1-Liver and PCSK9-low KPC cells showed high

uptake of fluorescently labelled Dil-LDL as measured by flow cytometry (Extended Data Fig. 4a,b) and immunofluorescence staining of lysosomal localized Dil-LDL (Extended Data Fig. 4c–f), relative to C2-Lung PCSK9-high cells, which had minimal uptake. Moreover, filipin staining, which visualizes cellular cholesterol depots, revealed high levels of lysosomal cholesterol in C1-Liver lines consistent with high cholesterol uptake rates, whereas C2-Lung lines predominantly displayed plasma membrane cholesterol and minimal lysosomal staining (Extended Data Fig. 4g–i). Low PCSK9, high LDL uptake and lysosomal cholesterol was also evident in cells isolated from KPC-derived liver metastases, relative to the matched isogenic primary PDAC cells (Extended Data Fig. 4j–n).

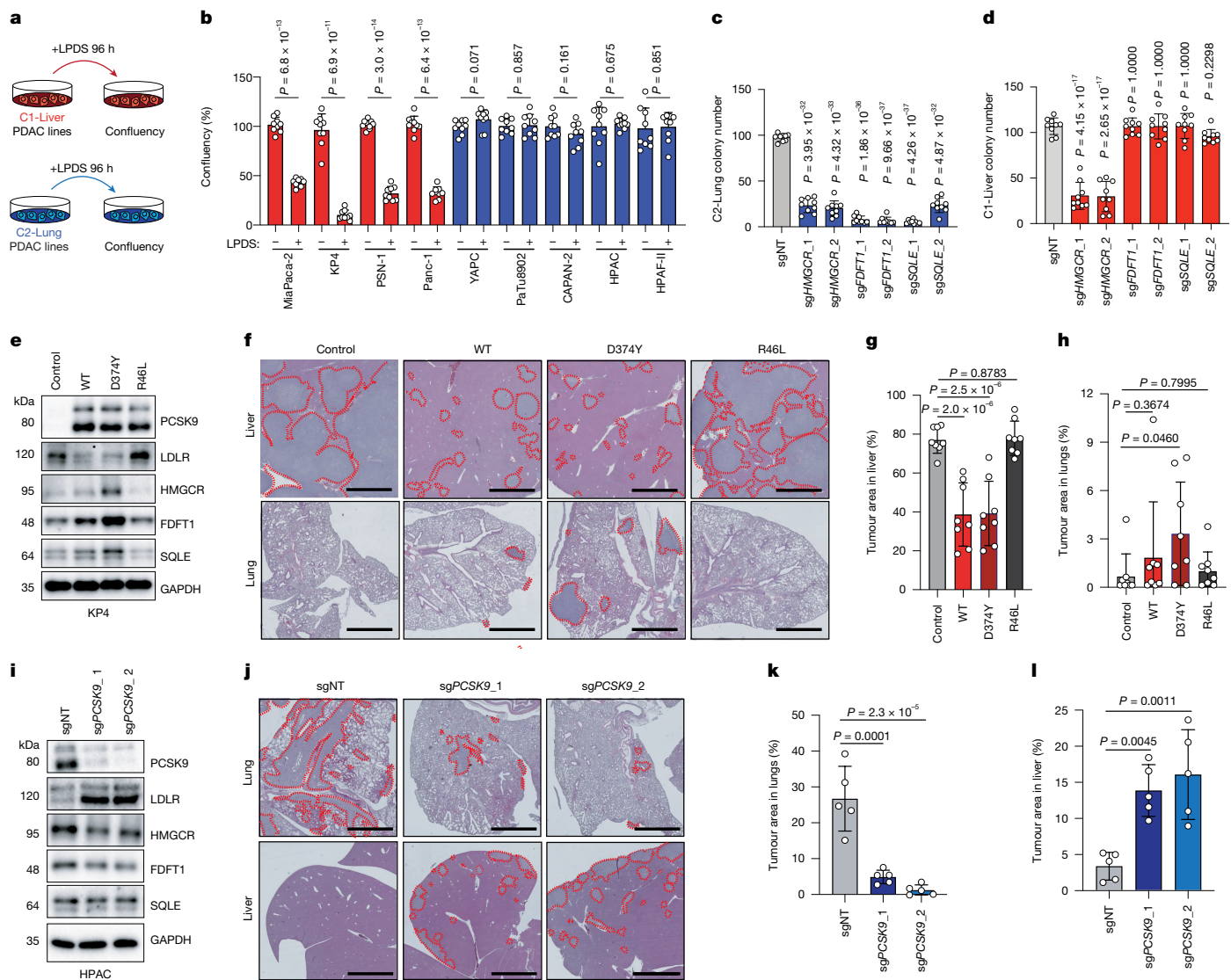


Fig. 3 | Differential cholesterol metabolism directs metastatic organ preference. **a**, Schematic depicting experiments utilizing LPDS. **b**, Percentage confluence of C1-Liver lines (red bars) and C2-lung lines (blue bars) following culture in LPDS for 96 h. Statistical significance was calculated using a two-tailed *t*-test. *n* = 9 replicates per condition. **c,d**, Quantification of C2-Lung line (**c**) and C1-Liver line (**d**) colony number following CRISPR-mediated knockout of the indicated cholesterol biosynthesis genes. Statistical significance was calculated using a one-way analysis of variance (ANOVA) with Bonferroni correction. *n* = 9 biological replicates. sgNT, non-targeting sgRNA; sgHMGCR, sgRNA targeting HMGCR; sgFDFT1, sgRNA targeting FDFT1; sgSQLE, sgRNA targeting SQLE. **e**, Immunoblot of the indicated proteins in KP4 cells expressing PCSK9 variants: wild-type (WT), active variant (D374Y) and inactive variant (R46L). **f**, Representative H&E images of liver (top) four weeks post intrasplenic injection

LDL uptake was essential for sustaining C1-Liver cell viability but not for C2-Lung cells. Specifically, C1-Liver cells and PCSK9-low KPC cells showed reduced proliferation following 96 h of culture in lipoprotein-depleted serum (LPDS), whereas the growth of C2-Lung lines was unaffected (Fig. 3a,b and Extended Data Fig. 5a). In response, C1-Liver lines upregulated cholesterol biosynthesis pathway enzymes via SCAP-SREBP feedback^{28,29} (Extended Data Fig. 5b,c); while C2-Lung lines did not (Extended Data Fig. 5c,d). Supplementation with exogenous LDL or cholesterol was sufficient to rescue growth of C1-Liver lines grown in LPDS, indicating that loss of LDL-cholesterol is the primary mediator of the observed growth impairment (Extended Data Fig. 5e,f).

and lungs (bottom) five weeks post tail vein injection of KP4 cells expressing the indicated PCSK9 variants. Tumour lesions are outlined in red. *n* = 8 mice per group. Scale bars, 500 μ m. **g,h**, Percentage tumour area in the liver (**g**) and lungs (**h**) from samples shown in **f**. Statistical significance was calculated using a one-way ANOVA using correction for least significant difference. **i**, Immunoblot of the indicated proteins in HPAC cells following CRISPR-mediated knockout of PCSK9 with two independent sgRNAs (sgPCSK9). **j**, Representative H&E images of lungs (top) four weeks post tail vein injection and liver (bottom) five weeks post intrasplenic injection of HPAC cells following CRISPR-mediated knockout of PCSK9. *n* = 5 mice per group. Scale bars, 500 μ m. **k,l**, Percentage tumour area in the lungs (**k**) and liver (**l**) from samples shown in **j**. Statistical significance was calculated using one-way ANOVA with Bonferroni correction. Error bars represent s.d. For gel source data, see Supplementary Fig. 1.

Similar to lipoprotein depletion, CRISPR-mediated knockout of LDLR also led to a compensatory upregulation of cholesterol biosynthesis pathway enzymes (Extended Data Fig. 5g), was selectively detrimental to C1-Liver lines relative to C2-Lung lines (Extended Data Fig. 5h–j) and impaired growth of KP4 cells in the liver (Extended Data Fig. 5k,l).

PCSK9-high lung-avid cells synthesize cholesterol

Consistent with their low uptake of LDL-cholesterol, PCSK9-high C2-Lung lines showed increased expression of cholesterol biosynthesis genes, including the master transcriptional regulator SREBP2

(Extended Data Fig. 6a–d), a pattern that was also observed in patient lung metastases compared with liver lesions (Extended Data Fig. 6e,f). Liver metastases also displayed lower expression of cholesterol biosynthesis genes relative to the primary tumour (Extended Data Fig. 6g). Moreover, DepMap data revealed that high *PCSK9* expression correlated with dependency on late-stage cholesterol biosynthesis genes in PDAC (Extended Data Fig. 6h). Accordingly, knockout of *FDFT1* and *SQLE* impaired growth of C2-Lung lines but not C1-Liver lines, which rely on LDL-cholesterol uptake (Fig. 3c,d and Extended Data Fig. 6i–k). All lines were sensitive to HMG-CoA reductase (*HMGCR*) knockout, which catalyses the rate-limiting step of the mevalonate pathway, indicating a shared dependence on early mevalonate pathway intermediates (Fig. 3c,d and Extended Data Fig. 6i–k). This result is consistent with anti-tumour effects associated with genetic deletion of *SCAP* in a PDAC mouse model³⁰. Collectively, these findings suggest that C2-Lung cell lines rely on de novo synthesis to maintain cholesterol pools and cellular growth, whereas C1-Liver lines depend on LDL uptake.

PCSK9 drives secondary organ selection

To test whether PCSK9 levels directly influence organ-specific growth, we first engineered the liver-avid KP4 line to express wild-type PCSK9, a gain-of-function mutant (D374Y) or a loss-of-function variant (R46L)^{31,32} (Fig. 3e). Wild-type PCSK9 and PCSK9(D374Y) caused a decrease in LDLR levels (Fig. 3e), decreased LDL uptake (Extended Data Fig. 7a,b) and a shift towards de novo cholesterol biosynthesis, as evidenced by increased expression of mevalonate pathway enzymes (Fig. 3e). When transplanted into the liver or lungs, parental KP4 cells and KP4 cells expressing PCSK9(R46L) developed large tumours in the liver over a period of four to five weeks, whereas cells expressing wild-type PCSK9 or PCSK9(D374Y) exhibited reduced growth in the liver over the same time frame (Fig. 3f,g). Notably, whereas parental KP4 cells did not grow in the lungs, PCSK9(D374Y)-expressing cells were able to grow in the lungs (Fig. 3f,h).

We next tested whether knockout of PCSK9 or overexpression of LDLR in a C2-Lung line, HPAC, was sufficient to enable growth within the liver. CRISPR-mediated knockout of PCSK9 increased the amount of LDLR protein and LDL uptake and reduced cholesterol biosynthesis gene expression (Fig. 3i and Extended Data Fig. 7c,d) without affecting in vitro growth (Extended Data Fig. 7e). However, upon tail vein injection, PCSK9-knockout cells displayed reduced growth in the lungs and enhanced growth in the liver relative to control HPAC cells treated with non-targeting single guide RNA (sgRNA) (Fig. 3j–l). Similarly, overexpression of LDLR in HPAC cells phenocopied PCSK9 suppression (Extended Data Fig. 7f–i) and led to increased growth in the liver (Extended Data Fig. 7j,k). Finally, CRISPR-mediated *Pcsk9* knockout in mouse PDAC cells transplanted into syngeneic hosts also lead to decreased growth in the lungs and increased growth in the liver (Extended Data Fig. 7l–s), with no effect on primary pancreatic tumour growth (Extended Data Fig. 7t,u). These findings support a model whereby PCSK9–LDLR status and the associated cholesterol uptake versus synthesis are necessary and sufficient to determine whether PDAC cells grow in the liver or the lungs, respectively.

Our findings show that baseline levels of PCSK9 predict secondary organ preference, especially in patients with liver-only or lung-only metastases (see Fig. 2h). However, PCSK9-high and PCSK9-low cells can coexist within the same primary tumour (Extended Data Fig. 8a,b). Since PDAC cells can reach both the liver and lungs regardless of PCSK9 status (see Fig. 1l–n), we tested whether PCSK9 expression still predicts colonization in heterogeneous tumours. Using mouse MT23 cells (shown in Extended Data Fig. 4j), which form primary tumours with variable PCSK9 expression, we found that liver metastases uniformly expressed low PCSK9, whereas lung metastases showed high expression (Extended Data Fig. 8a,b). These results confirm that PCSK9 status reliably predicts organ-specific colonization and tumour burden in the liver or the lungs.

Sterol dependencies of liver-avid cells

We next sought to determine the fate of the LDL-cholesterol actively taken up by C1-Liver cells, and its specific role in promoting survival and colonization of the liver. Lysosomal cholesterol is a critical mediator of proliferative signalling via activation of the master nutrient sensor mTORC1 (refs. 33,34). Filipin staining confirmed high lysosomal cholesterol in C1-Liver cells, which was reduced by lipoprotein depletion (Fig. 4a and Extended Data Fig. 9a), leading to reduced phosphorylation of the downstream mTORC1 substrates p70S6K and 4EBP1 (Fig. 4b). By contrast, C2-Lung lines, which lack measurable lysosomal cholesterol stores, maintained mTORC1 signalling independent of exogenous lipoprotein (Fig. 4a,b and Extended Data Fig. 9a). However, PCSK9 knockout in the C2-Lung line HPAC restored LDL uptake and made mTORC1 activation lipoprotein-dependent in these cells (Extended Data Fig. 9b). Additionally, liver tumours derived from PCSK9-knockout HPAC cells showed higher mTORC1 activity relative to equivalent tumours growing in the lungs, as shown by immunofluorescence staining of tumour sections for phosphorylated ribosomal protein S6 (a downstream target of mTORC1) (Extended Data Fig. 9c). These data indicate that a function of PCSK9-low status and subsequent LDL-cholesterol uptake and lysosomal routing is to maintain proliferative competence in C1-Liver lines, at least in part by sustaining pro-growth mTORC1 signalling. Consistent with this model, DepMap reverse phase protein array (RPPA) data confirmed a positive correlation between liver colonization potential and mTOR activity (Fig. 4c), and patient liver metastases had higher phosphorylated S6 than lung lesions (Fig. 4d). Conversely, high *PCSK9* mRNA levels correlated with lower mTOR activity (Extended Data Fig. 9d), supporting a model in which low PCSK9 promotes liver growth via LDLR-mediated cholesterol uptake and mTORC1 activation.

Following its export from the lysosome, cholesterol can be partly converted to oxysterols by the action of specific cytochrome P450 enzymes. In turn, release of oxysterols relieves potential cholesterol overload in the producing cells and can exert modulatory functions on the surrounding tissue, including effects that promote tumour growth and metastasis³⁵. We therefore assessed whether C1-Liver cells express enzymes required for oxysterol production. Quantitative PCR with reverse transcription (RT-qPCR) revealed that the mRNA level of *CYP46A1*, which encodes a cholesterol hydroxylase that synthesizes 24(S)-hydroxycholesterol (24-HC), was upregulated in C1-Liver cell lines and inversely correlated with PCSK9 expression in The Cancer Genome Atlas (TCGA) PDAC dataset (Fig. 4e and Extended Data Fig. 9e,f). Other cholesterol hydroxylases showed no correlation with PCSK9 status (Extended Data Fig. 9g), suggesting a specific role for *CYP46A1* in C1-Liver cells. In support of this idea, high *CYP46A1* expression was correlated with increased liver invasion potential in PDAC cells (Fig. 4f).

Studies in the brain have shown that 24-HC, which is synthesized and secreted by neuronal cells, can promote activation of lipoprotein synthesis and cholesterol efflux genes in neighbouring astrocytes via the nuclear hormone receptor liver X receptor (LXR)^{36,37}. Given that hepatocytes are the primary source of LDL-cholesterol synthesis in the liver, we tested whether an analogous tumour–hepatocyte circuit may also exist during colonization of the liver. To do so, we measured activation of LXR target genes in primary mouse hepatocytes following incubation for 24 h with conditioned medium isolated from KP4 (C1-Liver) or HPAC (C2-Lung) cells (Fig. 4g). Only conditioned medium from KP4 cells activated LXR target genes (*ABCA1*, *ABCG1*, *LXRA*, *PLTP*, *SREBF1* and *APOE*) in mouse hepatocytes (Fig. 4h). Similarly, treatment with KP4-conditioned medium but not HPAC-conditioned medium led to a decrease in hepatocyte cholesterol levels (Extended Data Fig. 9h), suggesting an increased rate of cholesterol efflux occurs in response to KP4-conditioned medium in hepatocytes.

The ability of KP4-conditioned medium to activate LXR target genes and cholesterol efflux in hepatocytes was lost upon *CYP46A1* knockout in KP4 cells, indicating that this response is dependent on *CYP46A1*

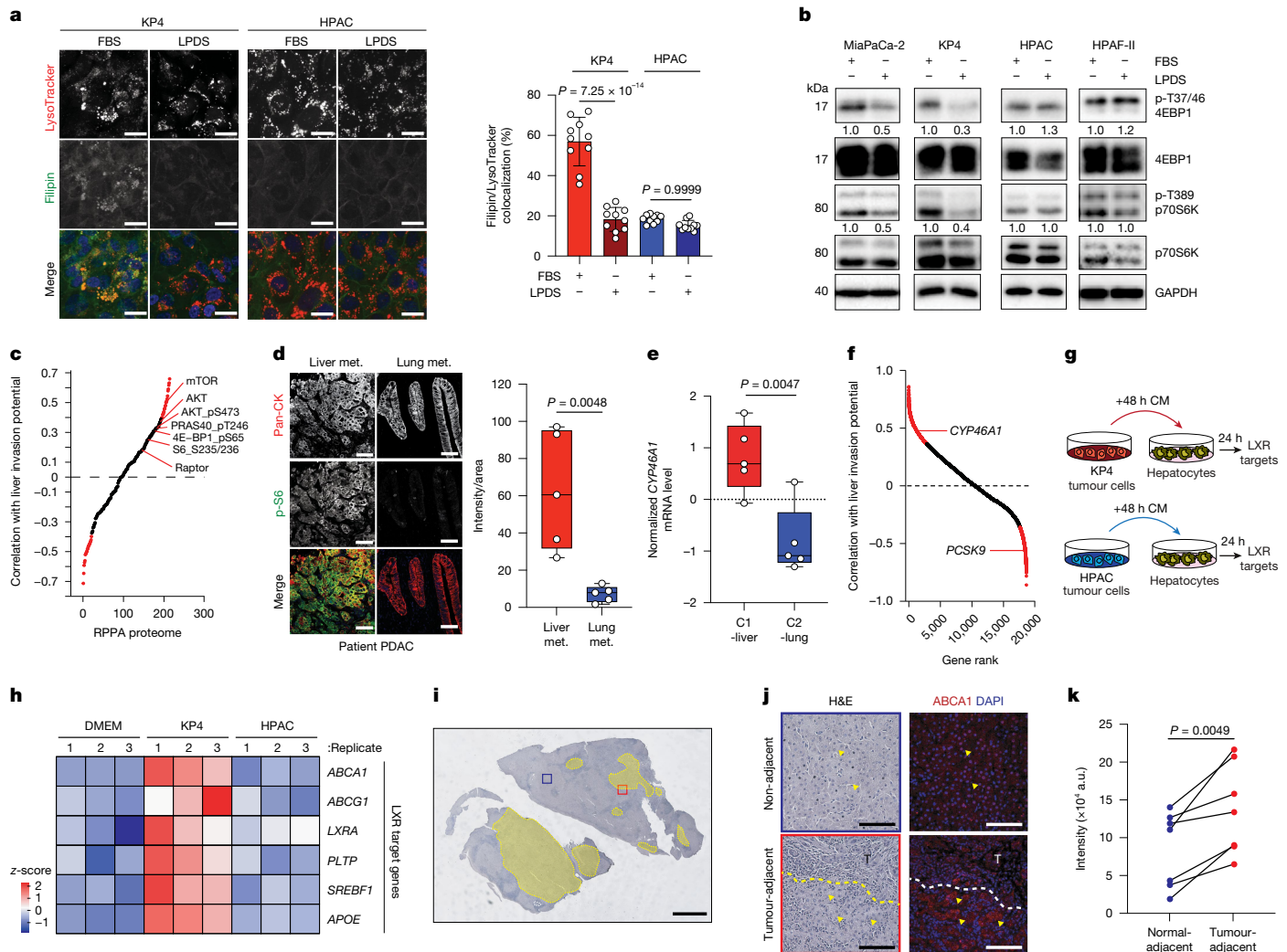


Fig. 4 | Liver-avid cells utilize cholesterol to activate mTORC1 and condition the microenvironment. **a**, Representative immunofluorescence images (left) and quantification (right) of lysosomal cholesterol in KP4 and HPAC cells grown in media containing fetal bovine serum (FBS) or LPDS for 72 h. Statistical significance was calculated using a one-way ANOVA followed by pairwise *t*-tests with Bonferroni correction. Error bars depict s.d. $n = 10$ fields per condition from 3 biological replicates. Scale bars, 10 μ m. **b**, Immunoblot for the indicated proteins in cells grown as in **a**. Numbers underneath indicate normalized densitometry. **c**, Analysis of RPPA data identifies mTOR and mTOR targets as positively correlated with liver invasion potential. **d**, Representative immunofluorescence images (left) and quantification (right) of phosphorylated S6 (Ser240/244; p-S6) in human PDAC liver and lung metastatic lesions (met.). Each point represents the mean intensity of at least ten fields from five liver and five lung metastases. Statistical significance was calculated using a two-tailed *t*-test. Pan-CK, pan-cytokeratin antibody labelling. Scale bars, 50 μ m. **e**, RT-qPCR measurement of *CYP46A1* mRNA in C1-Liver ($n = 5$) and C2-Lung ($n = 5$) lines. Statistical significance was calculated using a two-tailed *t*-test. The centre

line represents the median, box edges delineate first and third quartiles and whiskers extend to minimum and maximum values. **f**, Gene expression correlation with relative liver invasion for 25 PDAC cell lines. Genes with significant positive (*CYP46A1*) or negative (*PCSK9*) correlations are shown in red. **g**, Schematic depicting conditioned media (CM) experiments. **h**, Heat map depicting LXR target gene expression (z-scores) in mouse hepatocytes following incubation with KP4 or HPAC-conditioned media for 24 h. Columns represent biological replicates. **i**, Representative H&E image of liver metastases. Yellow outlines indicate tumour regions. Blue and red boxes indicate non-adjacent and tumour-adjacent regions, respectively. Scale bar, 1 mm. **j**, Representative immunofluorescence images for ABCA1 in non-adjacent and tumour-adjacent regions. Dashed line indicates tumour (T) and adjacent liver margin. Arrowheads indicate hepatocytes. Scale bars, 100 μ m. **k**, ABCA1 staining intensity in tumour-adjacent (red) and non-adjacent (blue) regions. Data points represent the mean of $n = 10$ fields per sample from 7 samples. Statistical significance was calculated using a two-tailed *t*-test. For gel source data, see Supplementary Fig. 1.

(Extended Data Fig. 9i–k). Accordingly, addition of exogenous 24-HC was able to rescue LXR target gene expression in hepatocytes treated with medium conditioned by CYP46A1-knockout KP4 cells (Extended Data Fig. 9j). To assess whether LXR activation occurs in hepatocytes *in vivo*, tumour-adjacent and non-adjacent sections from liver metastases were stained for the LXR transcriptional target ABCA1 (Fig. 4i), a cholesterol exporter belonging to the ABC family of transporters. Tumour-adjacent hepatocytes expressed higher levels of ABCA1 relative to non-adjacent hepatocytes (Fig. 4j,k), suggesting that hepatocytes in proximity to tumour cells activate LXR target gene expression to a

higher degree than non-adjacent hepatocytes. These data suggest that C1-Liver derived 24-HC can condition the liver microenvironment in a feed-forward manner to support continued LDL-cholesterol supply, fuelling tumour growth. Consistent with this idea, CYP46A1 knockout reduced KP4 growth in the liver without affecting *in vitro* proliferation, whereas lung growth remained low and unchanged (Extended Data Fig. 9l–o). Thus, CYP46A1-mediated oxysterol signalling promotes liver-specific growth. Overall, increased LDL uptake in C1-Liver cells supports mTORC1-mediated growth and production of oxysterols that enhance the tumour-supportive niche.

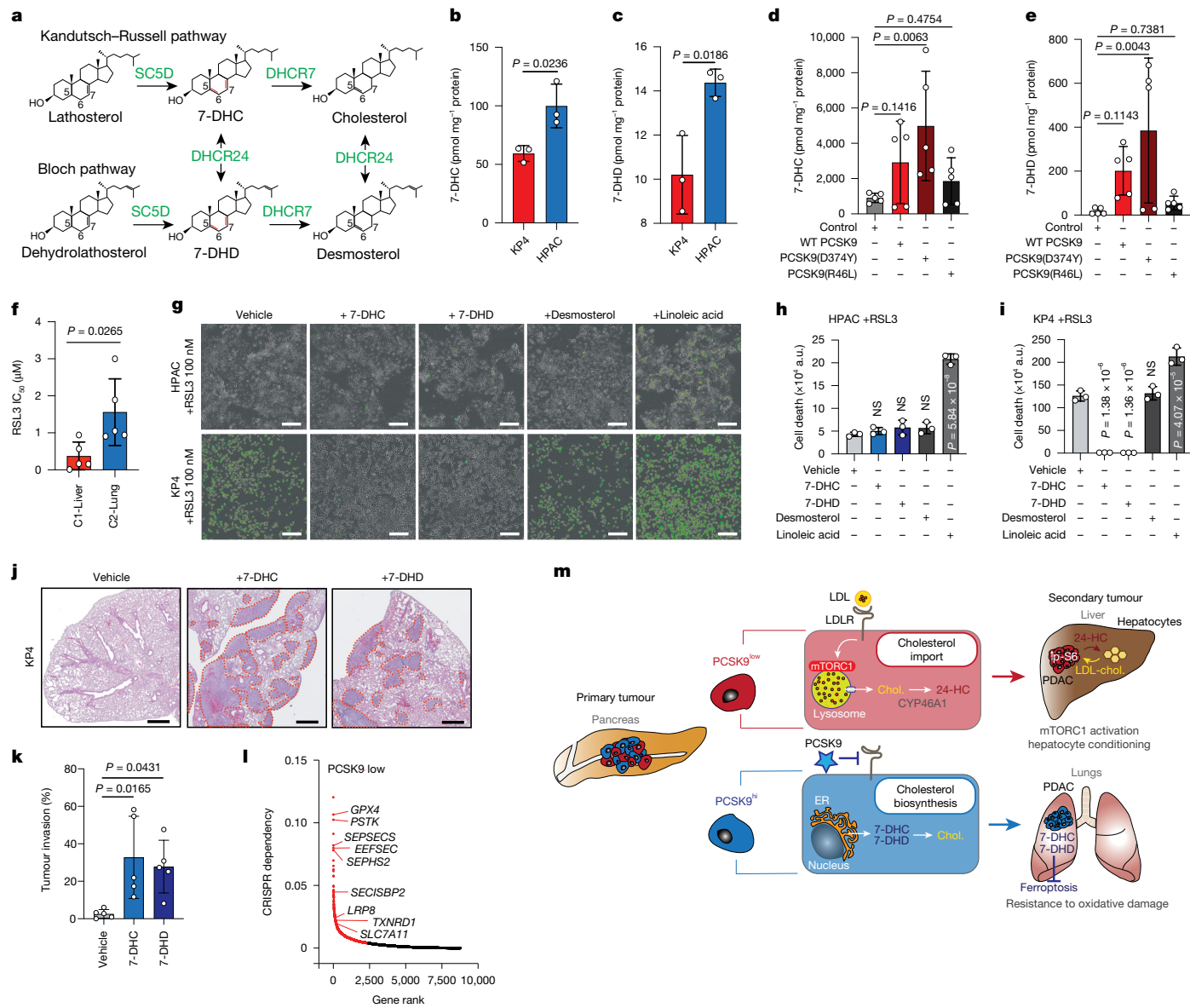


Fig. 5 | Lung-avid PDAC cells produce sterol intermediates with anti-ferroptotic properties. **a**, Schematic showing distal cholesterol biosynthesis steps that generate 7-DHC and 7-DHD. Enzymes are shown in green. Red lines indicate the 5,7-diene B ring structure. **b,c**, Measurement of 7-DHC (**b**) and 7-DHD (**c**) in the indicated cell lines. $n = 3$ biological replicates per cell line. Statistical significance was calculated using a two-tailed *t*-test. **d,e**, Measurement of 7-DHC (**e**) and 7-DHD (**f**) in KP4 cells expressing the indicated PCSK9 variants. $n = 5$ biological replicates per group. Statistical significance was calculated using a one-way ANOVA with least significant difference correction. **f**, Average RSL3 IC₅₀ measurement for C1-Liver ($n = 5$) and C2-Lung ($n = 5$) lines. Statistical significance was calculated using a two-tailed *t*-test. **g**, Representative images depicting cell death (SYTOX Green) of HPAC (top) and KP4 (bottom) cells treated with RSL3 plus vehicle or the indicated lipids for 24 h. Scale bars, 200 μm. **h,i**, Quantification of the SYTOX

Green fluorescence shown in **g** for HPAC (**h**) and KP4 (**i**). Statistical significance for comparison with vehicle-only control was calculated using a one-way ANOVA with Bonferroni correction. $n = 3$ biological replicates per condition. **j**, Representative H&E staining showing tumour burden in the lungs two weeks post tail vein injection of KPC1 cells following pre-treatment with sterols or vehicle. Tumour lesions are outlined in red. Scale bars, 1 mm. **k**, Percentage tumour area in the lungs from samples shown in **j**. $n = 5$ mice per condition. Statistical significance was calculated using a one-way ANOVA with Bonferroni correction. **l**, DepMap CRISPR dependency ranking of top genes associated with PCSK9-low status across all cancers. $n = 1,005$ cell lines. **m**, Model depicting how PCSK9-dependent regulation of cholesterol (chol.) import (top) and biosynthesis (bottom) regulates metabolic fitness for growth in the liver and lungs, respectively. All error bars represent s.d. of the mean. ER, endoplasmic reticulum; NS, not significant.

Sterol dependencies of lung-avid cells

Finally, we sought to determine how increased de novo synthesis of cholesterol intermediates driven by high PCSK9 levels contributes to lung colonization by PDAC cells. Recent studies have shown that resistance to ferroptosis—an iron-dependent form of cell death involving phospholipid peroxidation³⁸—is mediated by several late-step cholesterol synthesis intermediates including squalene³⁹ and 7-dehydrocholesterol

(7-DHC)^{40–42}. The 5,7-diene B ring structure of 7-DHC functions as a radical-trapping agent that suppresses ferroptosis^{40–42}, and sterols with similar structural features, such as 7-dehydrodesmosterol (7-DHD), also have anti-ferroptotic capabilities (Fig. 5a). High expression of sterol C5-desaturase (SC5D), 7-DHC reductase (DHCR7) and DHCR24 expression, along with several other distal cholesterol biosynthesis pathway enzymes, positively correlated with PCSK9-high status in samples from patients with PDAC (Extended Data Fig. 10a) and in C2-Lung

lines (see Extended Data Fig. 6b). Targeted metabolomics confirmed higher 7-DHC and 7-DHD in HPAC (C2-Lung) versus KP4 (C1-Liver) cells (Fig. 5b,c) and expression of active PCSK9 (D374Y) in KP4 cells was sufficient to increase the levels of these sterols (Fig. 5d,e).

To test whether cholesterol biosynthesis influences ferroptosis sensitivity, we treated C1-Liver and C2-Lung PDAC lines with the GPX4 inhibitors RSL3 and ML210. C2-Lung lines were collectively more resistant, showing higher mean half-maximum inhibitory concentration (IC_{50}) values relative to C1-Liver lines (Fig. 5f and Extended Data Fig. 10b). Similarly, HPAC cells were relatively resistant to RSL3 treatment (Fig. 5g,h). Accordingly, HPAC cells resisted RSL3-induced death, as measured by SYTOX Green, whereas KP4 cells were highly sensitive—an effect that was reversed by adding exogenous 7-DHC or 7-DHD but not desmosterol (Fig. 5g,j). Addition of the polyunsaturated fatty acid linoleic acid enhanced RSL3-induced cell death in both KP4 and HPAC cells, but to a greater extent in KP4 cells (Fig. 5g–i). These findings suggest that intermediates of the distal cholesterol biosynthesis pathway protect C2-Lung cells from oxidative stress. Accordingly, knockout of PCSK9, or blocking the synthesis of 7-DHC and 7-DHD following knockout of SC5D, sensitized HPAC cells to GPX4 inhibitors (Extended Data Fig. 10c–e) and reduced lung colonization (Extended Data Fig. 10f,g).

In KP4 cells, expression of dominant active PCSK9(D374Y), which causes a shift towards cholesterol biosynthesis (Fig. 3e), reduced sensitivity to GPX4 inhibition (Extended Data Fig. 10h). Knockout of SC5D had no effect, consistent with the reduced reliance on sterol biosynthesis in these cells (Extended Data Fig. 10i,j). Notably, pre-treatment of liver-avid KPC1 cells with 7-DHC or 7-DHD for 24 h *in vitro* was sufficient to enhance lung colonization following tail vein injection (Fig. 5j,k).

Consistent with these findings, unbiased analysis of CRISPR dependency data across 1,005 cancer cell lines showed that PCSK9-low status is strongly associated with sensitivity to GPX4 loss and several additional ferroptosis-protective genes (Fig. 5l) as well as GPX4 inhibitors (Extended Data Fig. 10k). Together, these findings indicate that actively engaging cholesterol biosynthesis simultaneously provides anti-fertoptotic sterol intermediates that support lung colonization, whereas cells that lack this activity are more susceptible to oxidative stress-induced cell death.

Discussion

Most cancer cells exhibit increased synthesis, uptake and storage of lipids for growth and stress adaptation^{43–46}. The optimal balance between these various lipid-handling activities may be partly dictated by energetic constraints: cholesterol synthesis is energetically expensive, thus cholesterol biosynthesis pathway genes are subjected to feedback regulation to maintain the levels of this lipid within a defined range that is compatible with growth^{43,47}. Additionally, the mevalonate pathway and distal cholesterol synthesis pathways (the Bloch and Kandutsch-Russell pathways) produce several growth-promoting metabolites, including prenylation precursors, dolichol, ubiquinone⁴⁵ and anti-fertoptotic derivatives^{40–42}. Owing to the high plasticity and regulation of the mevalonate–cholesterol pathway, the relative contributions of its branches and outputs to various aspects of cancer cell growth have remained unclear. Our study demonstrates that the differential utilization of the mevalonate–cholesterol pathway by PDAC cells can be best understood in the context of colonization of metabolically diverse niches within the liver and lungs (Fig. 5m).

PCSK9 emerges as a key determinant of secondary organ colonization preference in PDAC. Although extensive studies of PCSK9, conducted in the context of cardiovascular disease, have uncovered its role as a master regulator of LDLR stability and LDL-cholesterol import, far less is understood about its roles in the altered metabolism of cancer cells⁴⁸. Here we demonstrate that the ability of PCSK9 to switch PDAC cell metabolism between cholesterol import (PCSK9-low status)

versus synthesis (PCSK9-high status), is sufficient to impart different colonization fates. A key finding is that PCSK9 levels determine not only cholesterol uptake versus synthesis, but also distinct usage of mevalonate–cholesterol intermediates and derivatives. Specifically, PCSK9-low liver-avid cells use lysosomal cholesterol to activate mTORC1 signalling and produce 24-HC, to reprogramme the liver microenvironment to support tumour growth. By contrast, PCSK9-high PDAC cells produce 7-DHC and 7-DHD, intermediates with powerful free radical-trapping capabilities, to protect against ferroptosis in the oxygen-rich environment of the lung. This finding explains why liver-avid cells grow less efficiently in the lung, as they show limited production of these intermediates. Accordingly, increasing the amount of PCSK9 in liver-avid cells, which causes a shift towards cholesterol biosynthesis, enables their growth in the lung. Similarly, pre-treatment of liver-avid cells with exogenous 7-DHC or 7-DHD is sufficient to promote growth in the lung. Conversely, exclusive reliance on cholesterol biosynthesis—an oxygen-dependent process—may preclude PCSK9-high lung-avid cells from efficient colonization of the liver, which is characterized by zonal oxygen and metabolite distributions⁴⁹. Accordingly, ablation of PCSK9 or ectopic LDLR expression in lung-avid cells causes a shift towards cholesterol import and enables growth in the liver. Of note, our findings also highlight an innate ability of all cancer cells to seed within both the liver and lungs—however, the efficiency of outgrowth is dictated by PCSK9 status. Thus, whereas tumour cell-intrinsic PCSK9 status may be predictive of metastatic colonization site, adaptive changes in PCSK9 status over time may also enable growth at these sites. Overall, our findings establish PCSK9 as necessary and sufficient for secondary organ site colonization and highlight how differential modes of cholesterol acquisition and utilization can enable growth in metabolically diverse metastatic niches (Fig. 5m).

A relationship between cholesterol metabolism and PDAC differentiation has been proposed based on prior transcriptional and function studies^{50–52}. For instance, high expression levels of cholesterologenic genes in PDAC cells correlates with the classical subtype and overall better prognosis^{50,52}, which we also observe in our study. Conversely, high levels of LDLR were associated with aggressive disease and an increased risk of PDAC recurrence⁵³. A switch from classical to basal differentiation was also shown to occur following deletion of *NSDHL*—a distal cholesterol biosynthesis gene required for generation of zymosterone—in a mouse model of PDAC⁵¹. Although our studies do not establish a direct link between GATA6-dependent differentiation state and PCSK9 expression, they do suggest that PCSK9 is an important node that regulates cholesterol status in parallel to PDAC subtype specific behaviours.

Several large-scale studies evaluating the potential benefit of cholesterol-lowering drugs (for example, statins) on cancer incidence and mortality have reported different findings based on population distribution, cancer type, duration of inhibitor use or pre-existing cardiovascular disease^{44,48,54–56}. Moreover, conflicting reports on the benefits of statin use as therapy for advanced cancer have made clinical translation of cholesterol-lowering agents challenging. However, a study evaluating advanced ovarian, lung and pancreatic cancer showed a significant correlation between statin use and decreased risk of mortality⁵⁷. Another study identified a germline PCSK9-activating mutation that correlated with increased incidence of breast cancer metastasis in women⁵⁸. However, in this study, host-derived—and not tumour-derived—PCSK9 was linked to increased metastatic competence and, unexpectedly, the downstream mechanism did not involve cholesterol. Together, these studies highlight the importance of understanding the tumour-versus-host functions of PCSK9 and its mechanisms of action across cancer types to most effectively deploy PCSK9 inhibitors.

Finally, our study suggests that a more nuanced manipulation of the cholesterol biosynthetic pathway could enable a greater ability to exploit specific vulnerabilities of cancer cell populations. For instance, interventions that block mTORC1 signalling or tumour cell–hepatocyte

cross talk by targeting 24-HC production or LXR activation could antagonize liver colonization. Similarly, the inability of liver-avid PDAC cells to generate 7-DHC and 7-DHD make them more vulnerable to ferroptosis inducing agents, a finding with potential clinical applications. Conversely, the increased dependency of lung-avid PDAC cells on 7-DHC and 7-DHD suggest that directly blocking their production may antagonize lung colonization.

Online content

Any methods, additional references, Nature Portfolio reporting summaries, source data, extended data, supplementary information, acknowledgements, peer review information; details of author contributions and competing interests; and statements of data and code availability are available at <https://doi.org/10.1038/s41586-025-09017-8>.

1. Gerstberger, S., Jiang, Q. & Ganesh, K. Metastasis. *Cell* **186**, 1564–1579 (2023).
2. Jin, X. et al. A metastasis map of human cancer cell lines. *Nature* **588**, 331–336 (2020).
3. Massague, J. & Obenauf, A. C. Metastatic colonization by circulating tumour cells. *Nature* **529**, 298–306 (2016).
4. Elia, I. & Haigis, M. C. Metabolites and the tumour microenvironment: from cellular mechanisms to systemic metabolism. *Nat. Metab.* **3**, 21–32 (2021).
5. Liu, K. H. et al. Lung metastases in patients with stage IV pancreatic cancer: prevalence, risk factors, and survival impact. *J. Clin. Med.* **8**, 1402 (2019).
6. Deep, A., Haque, S. U. & Olowokure, O. Pulmonary metastases in pancreatic cancer, is there a survival influence? *J. Gastrointest. Oncol.* **6**, E48–E51 (2015).
7. Downs-Canner, S. et al. The indolent nature of pulmonary metastases from ductal adenocarcinoma of the pancreas. *J. Surg. Oncol.* **112**, 80–85 (2015).
8. Yasukawa, M., Kawaguchi, T., Kawai, N., Tojo, T. & Taniguchi, S. Surgical treatment for pulmonary metastasis of pancreatic ductal adenocarcinoma: study of 12 cases. *Anticancer Res.* **37**, 5573–5576 (2017).
9. Link, J. M. et al. Ongoing replication stress tolerance and clonal T cell responses distinguish liver and lung recurrence and outcomes in pancreatic cancer. *Nat. Cancer* **6**, 123–144 (2025).
10. Cheung, E. C. et al. Dynamic ROS control by TIGAR regulates the initiation and progression of pancreatic cancer. *Cancer Cell* **37**, 168–182.e164 (2020).
11. Maddipati, R. et al. MYC levels regulate metastatic heterogeneity in pancreatic adenocarcinoma. *Cancer Discov.* **12**, 542–561 (2022).
12. Mucciolo, G. et al. EGFR-activated myofibroblasts promote metastasis of pancreatic cancer. *Cancer Cell* **42**, 101–118.e111 (2024).
13. Pommier, A. et al. Unresolved endoplasmic reticulum stress engenders immune-resistant, latent pancreatic cancer metastases. *Science* **360**, eaao4908 (2018).
14. Raghavan, S. et al. Microenvironment drives cell state, plasticity, and drug response in pancreatic cancer. *Cell* **184**, 6119–6137.e6126 (2021).
15. Tsanov, K. M. et al. Metastatic site influences driver gene function in pancreatic cancer. Preprint at *bioRxiv* <https://doi.org/10.1101/2024.03.17.585402> (2024).
16. Wang, X. et al. Identification of a subset of immunosuppressive P2RX1-negative neutrophils in pancreatic cancer liver metastasis. *Nat. Commun.* **12**, 174 (2021).
17. Bailey, P. et al. Genomic analyses identify molecular subtypes of pancreatic cancer. *Nature* **531**, 47–52 (2016).
18. Cancer Genome Atlas Research Network. Integrated genomic characterization of pancreatic ductal adenocarcinoma. *Cancer Cell* **32**, 185–203.e13 (2017).
19. Collisson, E. A. et al. Subtypes of pancreatic ductal adenocarcinoma and their differing responses to therapy. *Nat. Med.* **17**, 500–503 (2011).
20. Connor, A. A. et al. Integration of genomic and transcriptional features in pancreatic cancer reveals increased cell cycle progression in metastases. *Cancer Cell* **35**, 267–282.e267 (2019).
21. Moffitt, R. A. et al. Virtual microdissection identifies distinct tumor- and stroma-specific subtypes of pancreatic ductal adenocarcinoma. *Nat. Genet.* **47**, 1168–1178 (2015).
22. O’Kane, G. M. et al. GATA6 expression distinguishes classical and basal-like subtypes in advanced pancreatic cancer. *Clin. Cancer Res.* **26**, 4901–4910 (2020).
23. Aung, K. L. et al. Genomics-driven precision medicine for advanced pancreatic cancer: early results from the COMPASS trial. *Clin. Cancer Res.* **24**, 1344–1354 (2018).
24. Link, J. M. et al. Tumor-infiltrating leukocyte phenotypes distinguish outcomes in related patients with pancreatic adenocarcinoma. *JCO Precis. Oncol.* <https://doi.org/10.1200/PO.20.00287> (2021).
25. Boj, S. F. et al. Organoid models of human and mouse ductal pancreatic cancer. *Cell* **160**, 324–338 (2015).
26. Kruger, S. et al. Isolated pulmonary metastases define a favorable subgroup in metastatic pancreatic cancer. *Pancreatology* **16**, 593–598 (2016).
27. Zhang, S. et al. Single cell transcriptomic analyses implicate an immunosuppressive tumor microenvironment in pancreatic cancer liver metastasis. *Nat. Commun.* **14**, 5123 (2023).
28. Brown, M. S. & Goldstein, J. L. Cholesterol feedback: from Schoenheimer’s bottle to Scap’s MELADL. *J. Lipid Res.* **50**, S15–S27 (2009).
29. Brown, M. S., Radhakrishnan, A. & Goldstein, J. L. Retrospective on cholesterol homeostasis: the central role of Scap. *Annu. Rev. Biochem.* **87**, 783–807 (2018).
30. Ishida, C. T. et al. SREBP-dependent regulation of lipid homeostasis is required for progression and growth of pancreatic ductal adenocarcinoma. *Cancer Res. Commun.* **4**, 2539–2552 (2024).
31. Kotowski, I. K. et al. A spectrum of PCSK9 alleles contributes to plasma levels of low-density lipoprotein cholesterol. *Am. J. Hum. Genet.* **78**, 410–422 (2006).
32. Sarkar, S. K. et al. A transient amphipathic helix in the prodomain of PCSK9 facilitates binding to low-density lipoprotein particles. *J. Biol. Chem.* **295**, 2285–2298 (2020).
33. Castellano, B. M. et al. Lysosomal cholesterol activates mTORC1 via an SLC38A9–Niemann-Pick C1 signaling complex. *Science* **355**, 1306–1311 (2017).
34. Shin, H. R. et al. Lysosomal GPCR-like protein LYCHOS signals cholesterol sufficiency to mTORC1. *Science* **377**, 1290–1298 (2022).
35. Nelson, E. R. et al. 27-Hydroxycholesterol links hypercholesterolemia and breast cancer pathophysiology. *Science* **342**, 1094–1098 (2013).
36. Courtney, R. & Landreth, G. E. LXR regulation of brain cholesterol: from development to disease. *Trends Endocrinol. Metab.* **27**, 404–414 (2016).
37. Wang, B. & Tontonoz, P. Liver X receptors in lipid signalling and membrane homeostasis. *Nat. Rev. Endocrinol.* **14**, 452–463 (2018).
38. Dixon, S. J. & Olzmann, J. A. The cell biology of ferroptosis. *Nat. Rev. Mol. Cell Biol.* **25**, 424–442 (2024).
39. Garcia-Bermudez, J. et al. Squalene accumulation in cholesterol auxotrophic lymphomas prevents oxidative cell death. *Nature* **567**, 118–122 (2019).
40. Freitas, F. P. et al. 7-Dehydrocholesterol is an endogenous suppressor of ferroptosis. *Nature* **626**, 401–410 (2024).
41. Li, Y. et al. 7-Dehydrocholesterol dictates ferroptosis sensitivity. *Nature* **626**, 411–418 (2024).
42. Yamada, N. et al. Inhibition of 7-dehydrocholesterol reductase prevents hepatic ferroptosis under an active state of sterol synthesis. *Nat. Commun.* **15**, 2195 (2024).
43. Mullen, P. J., Yu, R., Longo, J., Archer, M. C. & Penn, L. Z. The interplay between cell signalling and the mevalonate pathway in cancer. *Nat. Rev. Cancer* **16**, 718–731 (2016).
44. Riscal, R., Skuli, N. & Simon, M. C. Even cancer cells watch their cholesterol! *Mol. Cell* **76**, 220–231 (2019).
45. Snaebjornsson, M. T., Janaki-Raman, S. & Schulze, A. Greasing the wheels of the cancer machine: the role of lipid metabolism in cancer. *Cell Metab.* **31**, 62–76 (2020).
46. Vasseur, S. & Guillaumont, F. Lipids in cancer: a global view of the contribution of lipid pathways to metastatic formation and treatment resistance. *Oncogenesis* **11**, 46 (2022).
47. Ye, J. & DeBose-Boyd, R. A. Regulation of cholesterol and fatty acid synthesis. *Cold Spring Harb. Perspect. Biol.* **3**, a004754 (2011).
48. Mahboobnia, K. et al. PCSK9 and cancer: rethinking the link. *Biomed. Pharmacother.* **140**, 111758 (2021).
49. Kietzmann, T. Metabolic zonation of the liver: the oxygen gradient revisited. *Redox Biol.* **11**, 622–630 (2017).
50. Daemen, A. et al. Metabolite profiling stratifies pancreatic ductal adenocarcinomas into subtypes with distinct sensitivities to metabolic inhibitors. *Proc. Natl. Acad. Sci. USA* **112**, E4410–E4417 (2015).
51. Gabitova-Cornell, L. et al. Cholesterol pathway inhibition induces TGF-β signaling to promote basal differentiation in pancreatic cancer. *Cancer Cell* **38**, 567–583.e511 (2020).
52. Karasinska, J. M. et al. Altered gene expression along the glycolysis–cholesterol synthesis axis is associated with outcome in pancreatic cancer. *Clin. Cancer Res.* **26**, 135–146 (2020).
53. Guillaumont, F. et al. Cholesterol uptake disruption, in association with chemotherapy, is a promising combined metabolic therapy for pancreatic adenocarcinoma. *Proc. Natl. Acad. Sci. USA* **112**, 2473–2478 (2015).
54. Jacobs, E. J., Newton, C. C., Thun, M. J. & Gapstur, S. M. Long-term use of cholesterol-lowering drugs and cancer incidence in a large United States cohort. *Cancer Res.* **71**, 1763–1771 (2011).
55. Nielsen, S. F., Nordestgaard, B. G. & Bojesen, S. E. Statin use and reduced cancer-related mortality. *N. Engl. J. Med.* **367**, 1792–1802 (2012).
56. Hillis, A. L. et al. Targeting cholesterol biosynthesis with statins synergizes with AKT inhibitors in triple-negative breast cancer. *Cancer Res.* **84**, 3250–3266 (2024).
57. Zhou, Q., Jiao, Z., Liu, Y., Devreotes, P. N. & Zhang, Z. The effects of statins in patients with advanced-stage cancers - a systematic review and meta-analysis. *Front. Oncol.* **13**, 1234713 (2023).
58. Mei, W. et al. A commonly inherited human PCSK9 germline variant drives breast cancer metastasis via LRP1 receptor. *Cell* **188**, 371–389.e28 (2025).

Publisher’s note Springer Nature remains neutral with regard to jurisdictional claims in published maps and institutional affiliations.

Springer Nature or its licensor (e.g. a society or other partner) holds exclusive rights to this article under a publishing agreement with the author(s) or other rightsholder(s); author self-archiving of the accepted manuscript version of this article is solely governed by the terms of such publishing agreement and applicable law.

© The Author(s), under exclusive licence to Springer Nature Limited 2025

Methods

Cell culture and reagents

MiaPaCa-2, KP4, PaTu8988T, PSN1, Panc-1, YAPC, PaTu8902, CAPAN-2, HPAC, HPAF-II and HEK 293T cell lines were obtained from the American Type Culture Collection (ATCC) or DSMZ. MT23 and MM10 cells were established from *Pdx1*^{Cre/+}; *Kras*^{LSL-G12D/+}; *Trp53*^{R172H/+} mice, backcrossed into a C57BL/6 background, and isolated from the pancreas and liver, respectively (provided by C.-I. Hwang). FC1245 (KPC1) were provided by D. Tuveson; HY15549 (KPC2) and HY16936 (KPC3) were provided by R. DePinho; MT3 (KPC4) were provided by C.-I. Hwang and D. Tuveson and were all derived from *Pdx1*^{Cre/+}; *Kras*^{LSL-G12D/+}; *Trp53*^{R172H/+} mice. All cell lines were cultured in DMEM (Gibco) supplemented with 10% FBS (Atlanta biologicals), 1% Penicillin/Streptomycin (Gibco) and 15 mM HEPES (Gibco) and grown in a humidified chamber at 37 °C, 5% CO₂. Cells were trypsinized using TrypLE (Gibco). Routine mycoplasma testing was performed using the Mycoplasma PCR detection kit (Abm, G238) at least once a month and the cell lines were authenticated by STR fingerprinting. Cell lines are passaged for a maximum of 15 passages upon thawing prior to replacement. Dil-LDL was purchased from ThermoFisher (L3482), filipin was purchased from Sigma (F9765-50MG), Lysotracker was purchased from ThermoFisher (L7528). LPDS was purchased from Kalen Biomed (880100-1). 24-hydroxycholesterol was purchased from Sigma (SML-1648). SYTOX Green was purchased from ThermoFisher scientific (S7020). 7-dehydrodesmosterol (EVU144) and desmosterol (EVU126) were purchased from Kerafast Inc, 7-dehydrocholesterol (30800-5G-F), linoleic acid (L1012-1G), oleic acid (O1383-1G), cholesterol (C3045-5G), mevalonolactone (M4667-1G), ML210 (SML0521-5mg) and LDL (L7914-5mg) were purchased from Sigma; RSL3 (HY-100218A) was purchased from MedChemExpress.

Plasmids

pLX304 Luciferase-V5 blast was a gift from K. Janes (Addgene plasmid #98580) and pAAV/D374Y-hPCSK9 was a gift from J. Bentzon (Addgene plasmid #58379). The D374Y-hPCSK9 variant was first cloned into pLJM1. To generate the wild-type and R46L PCSK9 variants, Quick-change mutagenesis (Agilent, 210519-5) was used to first correct the D374Y mutation (to generate wild-type PCSK9) and subsequently to introduce the R46L mutation. All constructs were validated by Sanger sequencing. LentiTet-LDLR-mCherry was a gift from R. Sherwood (Addgene plasmid #186739). The LDLR sequence was cloned into the pLJM1 backbone.

Lentiviral experiments

Lentivirus was produced by transfecting HEK 293T cells with lentiviral pLJM1 expression plasmids and packaging plasmids psPAX2 (Addgene plasmid #12260) and pMD2.G (Addgene plasmid #12259) at a ratio of 0.5:0.25 using X-tremeGENE transfection (Sigma-Aldrich, 6365787001) reagent following manufacturer's instructions. The supernatant containing the virus was collected after 48 h by passing through 0.45-µm filter to remove cellular debris. Target cells were infected with the virus-containing media using Polybrene reagent (EMD Millipore, TR-1003-G) following the manufacturer's protocol and selected for 48 h in 2 µg ml⁻¹ puromycin.

Immunoblotting

Cells were lysed in ice-cold buffer (50 mM HEPES, pH 7.4, 40 mM sodium chloride, 10 mM sodium pyrophosphate, 10 mM β-glycerophosphate, 50 mM sodium fluoride, 2 mM EDTA, and 1% Triton X-100) supplemented with protease inhibitor tablets (Fisher Scientific, A32965). Protein concentration was determined using a Pierce BCA protein assay kit (Life Technologies, 23227), and 20 µg of protein was resolved on 12% acrylamide gels and subsequently transferred onto PVDF membranes (EMD Millipore, IPVH00010). Following blocking with 5% skimmed milk in Tris-buffered saline with 0.2% Tween (TBS-T) (blocking buffer),

membranes were incubated overnight at 4 °C with primary antibodies in blocking buffer. The membranes were then washed three times with TBS-T and further incubated with species-specific horseradish peroxidase-conjugated secondary antibodies for 1 h in blocking buffer. Membranes were developed using SuperSignal West Pico chemiluminescent substrate (Fisher Scientific, 34080) and imaged with the ChemiDoc XRS+ system (Bio-Rad). Antibodies used are listed in Supplementary Table 7.

Proliferation assays

For clonogenicity assays, KP4 and MiaPaCa-2 cells were seeded at 2,000 cells per well, Panc-1 cells at 4,000 cells per well, and CAPAN-2, HPAC and HPAF-II cells at 8,000 cells per well in 6-well plates in growth media. After 10 days, the growth medium was aspirated, and cells were washed with PBS, fixed with ice-cold methanol for 10 min and stained with crystal violet solution (0.1% w/v) for 15 min at room temperature. For experiments using LPDS, cells were seeded in 96-well plates cells per well in growth media and allowed to grow for 24 h (KP4 and MiaPaCa-2 at 2,000 cells per well, Panc-1 at 4,000 cells per well, and CAPAN-2, HPAC and HPAF-II cells at 8,000 cells per well). Subsequently, the cells were washed with PBS and incubated in fresh growth media (DMEM, 10% FBS) or DMEM supplemented with 10% LPDS for 96 h. At the conclusion of the assay, the medium was aspirated, and cells were washed with PBS and fixed with ice-cold methanol for 10 min and stained with crystal violet solution (0.1% w/v). For proliferation assay with RSL3 and ML210 treatment, cells were seeded in 96-well plates (4,000 cells per well) and treated with different concentration of RSL3 for 96 h. Cells were then washed with PBS, fixed in ice-cold methanol, and stained with crystal violet solution (0.1%w/w).

SYTOX Green assay

Cells were seeded at a concentration of 4,000 cells per well in a 96-well plate and treated with the different lipid metabolites for 24 h at a concentration of 50 µM. RSL3/ML210 treatment was then added, and cell death was assessed using SYTOX Green (dilution 1:30,000) for the indicated time. Green staining area was imaged and quantified by Incucyte S3.

Immunohistochemistry

Slides were baked at 60 °C for 1 h, and paraffin removal was achieved through 2× 5 min washes in xylene, followed by sequential rehydration in ethanol (100, 90, 70, 50, and 30%) for 5 min each. After 2 water washes, samples were heat-treated for 20 min in a 10 mM sodium citrate buffer solution (pH 6.0), washed twice with PBS, and incubated for 30 min in methanol/5% hydrogen peroxide at room temperature to block endogenous peroxidase activity. Following 2× PBS washes, samples were blocked with 2.5% normal goat serum (NGS) for 1 h and then incubated overnight with primary antibody (Supplementary Table 7) at 4 °C. Subsequently, 2× 5 min PBS washes preceded incubation with secondary antibody. After 3 washes, slides were stained with di-aminebenzidine (DAB) substrate kit (Vector Laboratories, SK-4100) for 10 min, washed in water, and counterstained with haematoxylin before dehydration and mounting. Brightfield images were captured using a KEYENCE BZ-X710 microscope. Tumour sections were evaluated for staining positivity by a pathologist (K.W.W.) and quantified using a modified histoscore ranging from 1 to 5 (1, absent; 2, weak; 3, moderate; 4, strong; 5, very strong).

Immunofluorescence

Human and mouse cells were cultured on fibronectin-coated coverslips for 2 days after which cells were fixed with 4% paraformaldehyde (PFA) for 15 min at room temperature, permeabilized with 0.1% saponin, and blocked with NGS for 15 min. Subsequently, samples were incubated overnight at 4 °C with primary antibodies (Supplementary Table 7), then washed three times with PBS and incubated with secondary antibodies (Supplementary Table 7) at room temperature for 1 h. Coverslips were

Article

then mounted on glass slides using DAPI Fluoromount-G (Southern Biotech, 0100-20), except for filipin experiments where cells were incubated with SYTOX Green (ThermoFisher, S7020) for 10 min, washed three times, and directly mounted with Fluoromount-G (Southern Biotech, 0100-01). For Dil–LDL uptake assays, cells were cultured in serum-free medium for 16 h prior to incubation on ice for 30 min with Dil–LDL (ThermoFisher Scientific, L3482). The medium was then replaced with warmed fresh growth medium, and cells were transferred to a 37 °C incubator for 30 min. At the conclusion of the assay, coverslips were fixed and permeabilized as above and counterstained for LAMP2 and DAPI. For visualization of cholesterol, cells were first incubated with Lysotracker Red DND-99 (ThermoFisher Scientific, L7528) at a concentration of 100 nM for 30 min at 37 °C. Cells were then fixed with 4% PFA, permeabilized with 0.1% saponin and subsequently incubated with filipin (200 µg ml⁻¹) for 30 min at room temperature. After incubation, cells were washed with PBS and incubated with SYTOX Green (ThermoFisher, S7020) at a dilution of 1:10,000 to label specific nuclei and mounted using Fluoromount-G mounting medium (Southern Biotech, 0100-01).

Immunofluorescence of tissue sections was performed by first baking the samples at 60 °C for 1 h, followed by paraffin removal through two 5 min xylene washes and sequential rehydration in ethanol (100, 90, 70, 50, and 30%) for 5 min each. After 2 water washes, samples were heat-treated for 20 min in a 10 mM sodium citrate buffer solution (pH 6.0), washed twice with PBS, and then incubated for 30 min in methanol at room temperature, followed by 2 PBS washes. Blocking was performed with 2.5% NGS for 1 h after which samples were incubated overnight with primary antibody at 4 °C (Supplementary Table 7). After 2× 5 min PBS washes, samples were incubated with the secondary antibody and mounted with DAPI Fluoromount-G. Stained cells and tissue sections were visualized using a Zeiss LSM900 Axio Observer Z1/7.

RNA extraction and quantitative PCR

Total RNA was isolated using PureLink RNA mini kit (ThermoFisher, 12183025). cDNA synthesis was performed using the iScript reverse transcription supermix (Bio-Rad, 1708841), followed by real-time quantitative PCR using iTaq universal SYBR Green Supermix (Bio-Rad, 1725122) on a CFX384 Touch Real Time PCR Detection System (Bio-Rad). Primers used are detailed in Supplementary Table 8.

CRISPR knockout

CRISPR knockouts were generated employing the ribonucleoprotein-electroporation method as previously outlined⁵⁹. In brief, 200,000 cells were electroporated using an Amaxa 4D Nucleofector kit (Lonza, V4XC-9064). The guide RNA and Cas9 were complexed using IDT Cas9 and guides designed by Synthego. After 3–4 days, cells were expanded, and gene depletion was assessed 7 days post-electroporation via western blot analysis and/or sequencing. Guide RNA sequences can be found in Supplementary Table 9.

PCSK9 ELISA

The concentration of PCSK9 in the conditioned media of PDAC cells was determined using the Human Proprotein Convertase 9 (PCSK9) Quantikine ELISA Kit from R&D Systems (DPC900), following the manufacturer's instructions. In brief, conditioned media from human PDAC cells were collected 24 h after media change, centrifuged at low speed to remove cellular debris and used in the ELISA assay.

Flow cytometry

Cells grown *in vitro* were detached and resuspended in ice-cold PBS and incubated with APC-conjugated LDLR antibody (Abcam, ab275614) at a concentration of 0.1 mg ml⁻¹ for 30 min on ice, protected from light. Following antibody incubation, cells were washed with PBS to remove unbound antibody. After the final wash, cells were resuspended in PBS for flow cytometry analysis. To measure Dil–LDL uptake, cells were

incubated with 5 µg ml⁻¹ Dil–LDL for 30 min. Cells were then detached, resuspended in ice-cold PBS, and washed twice with PBS to remove excess Dil–LDL. Following the final wash, cells were resuspended in PBS. Cells were analysed using a FACS Fortessa flow cytometer (BD Biosciences) equipped with appropriate lasers and filters for APC detection. Data were acquired using BD LSR Fortessa FACS Diva (version 9.0) software and analysed using FlowJow. Appropriate gating strategies were applied to exclude debris and ensure accurate analysis of single cells. Data were expressed as mean fluorescence intensity.

For analysis of mCherry or eGFP-expressing tumours, excised livers and lungs were washed twice with 10 ml HBSS and minced aseptically with a sterile razor blade on a 10-cm dish. Minced tissue was transferred to a flask containing 10 ml DMEM supplemented with 2.6 U ml⁻¹ Liberase DH and 1× antibiotic-antimycotic. Samples were digested on a bench-top stirrer at 37 °C for 1 h. Following digestion, tissue homogenates were transferred to 50-ml Falcon tubes and centrifuged at 1,000 rpm for 5 min at 4 °C. Pellets were resuspended in PBS and processed using the 37C_m_TDK1 program on the gentleMACS Tumor Dissociation according to the manufacturer's instructions. Once the program was complete, samples were centrifuged at 1,300 rpm for 5 min. Pellets were resuspended in 10 ml HBSS/2% FBS, washed, and centrifuged again. Cells were then resuspended in 5 ml HBSS/2% FBS and filtered through a 100-µm cell strainer into a new 50-ml conical tube. Next, 5 ml of RBC lysis buffer was added to the samples, which were incubated at room temperature for 5 min. The reaction was quenched with 10 ml HBSS/2% FBS, and the samples were centrifuged. Cells were analysed using a FACS Fortessa flow cytometer (BD Biosciences) equipped with appropriate lasers and filters for mCherry and eGFP detection. Data were acquired using BD LSR Fortessa FACS Diva (version 9.0) software and analysed using FlowJow. Appropriate gating strategies were applied to exclude debris and ensure accurate analysis of single cells. Data were expressed as log₂ fold change of the percentage of positive mCherry or eGFP cells.

Metabolomics

Cell pellets were collected and suspended in 500 µl of water:methanol:chloroform (1:5:2) in Eppendorf tubes. The samples were homogenized on a MM 400 mill mixer with the aid of 2× 3-mm metal balls and at a shaking frequency of 30 Hz for 3 min. The homogenization step was repeated 2 more times. The samples were then ultra-sonicated in an ice-water bath for 2 min and subsequently centrifuged at 21,000g and 5 °C for 10 min. The clear supernatants were collected for LC–MS analysis and the precipitated pellets were used for protein assay by UV-VIS spectroscopy using a standardized Bradford procedure. Serially diluted standard solutions of 7-dehydrocholesterol and 7-dehydrodesmosterol were prepared in acetonitrile. One-hundred microlitres of the supernatant of each sample was mixed with 300 µl of 50% methanol and 150 µl of chloroform. After vortex mixing and centrifugal clarification, the organic phase was collected and dried under a gentle nitrogen gas flow. The residue was dissolved in 100 µl of acetonitrile. To each 50 µl of each sample solution or each standard solution, 450 µl of 4-phenyltriazoline-3,5-dione solution was added. The mixtures were incubated at room temperature for 2 h on a Thermomixer at 600 rpm. Ten-microlitre aliquots of the resultant solutions were injected into a C18 UPLC column to a UPLC-MRM/MS on an Agilent 1290 UHPLC system coupled to Sciex 7500 QQQ mass spectrometer operated in the positive ion ESI mode using 0.1% formic acid in water and 0.1% formic acid in acetonitrile as the mobile phase for binary solvent gradient elution under optimized operation conditions. Concentrations of the compounds detected in the samples were calculated by interpolating their constructed linear regression calibration curves with internal standard calibration or external standard calibration.

In vivo experiments

To evaluate organ seeding and growth of human PDAC cell lines, 500,000 luciferase-positive cells (KP4, Panc-1, HPAC and HPAF-II)

were injected into NOD-*scid*-IL2R γ ^{null} (NSG) mice (Jackson Labs, 005557) via intrasplenic or tail vein injection to target the liver and the lungs, respectively. Bioluminescence imaging following administered of 30 mg kg⁻¹ luciferin via intraperitoneal injection was performed weekly and imaged using an IVIS Spectrum over the duration of four weeks to monitor tumour development and progression. To measure spontaneous seeding and colonization, the same number of luciferase-positive cells were injected via intracardiac injection into the left ventricle of NSG mice and tumour burden was assessed 3 weeks post-injection. Images were quantified using the Living Image software. At the end point of the experiments, tissue samples were collected and immediately fixed in 10% formalin. Following fixation, tissues were embedded in paraffin and 5-μm sections were cut and subjected to H&E staining. Tumour regions within the stained tissue sections were identified based on morphological features. The percentage tumour invasion for each organ was calculated as a percentage of the total tissue area.

For intracardiac injection experiments, tumour infiltration in the lung and liver from the same mice was calculated as a colonization ratio using this formula:

$$\text{Liver : lung ratio} = \log_2 \frac{\text{liver tumour infiltration}(\%)}{\text{lung tumour infiltration}(\%)}$$

To evaluate PCSK9 abundance after organ seeding, 100,000 luciferase-positive KPC-derived cells (MT23), were injected via intrasplenic or tail vein injection or orthotopically to target the liver, the lungs and the pancreas respectively into C57BL/6J mice (Jackson Labs, 000664). Bioluminescence imaging following administered of 30 mg kg⁻¹ luciferin via intraperitoneal injection was performed weekly using an IVIS Spectrum to monitor the development and progression of tumours. Two weeks post-injection, tissue samples were collected and immediately fixed in 10% formalin. Following fixation, tissues were embedded in paraffin and 5-μm sections were cut. Tumour regions within the stained tissue sections were identified using CK19 antibody and PCSK9 abundance was evaluated. Experiments using KPC1-4 cells involved identical injection into C57BL/6J mice using the procedures described.

To evaluate the effect of 7-DHC and 7-DHD on tumour growth, KPC1 murine pancreatic cancer cells were cultured in DMEM supplemented with 10% fetal bovine serum (FBS) and 1% penicillin-streptomycin under standard conditions (37 °C, 5% CO₂). 24 h prior to injection, cells were treated as follows: vehicle (ethanol), 50 μM 7-dehydrocholesterol (7-DHC) dissolved in vehicle, and 50 μM 7-dehydrodesmosterol (7-DHD) dissolved in vehicle. After 24 h of treatment, 100,000 cells were collected, resuspended in 100 μl sterile PBS, and injected via the tail vein to seed the lungs of C57BL/6 mice. Mice were sacrificed 2 weeks post-injection. The lungs were collected, fixed in 10% formalin for 24 h, and embedded in paraffin. Tissue sections (5 μm) were stained with H&E following standard protocols. Stained slides were examined under light microscopy to assess tumour burden.

For cell mixing experiments, KP4-mCherry cells and HPAC-eGFP cells were cultured and collected at approximately 70% confluence. For each mouse, 250,000 KP4-mCherry cells were mixed with an equal number of HPAC-eGFP cells in sterile PBS. To target the liver and lungs of NSG mice, cells were injected via intrasplenic or tail vein injection, respectively. Mice were euthanized 2 weeks post-injection.

This study utilized six-week-old male and female mice. The maximum tumour size permitted was one cubic centimetre, and endpoints of all experiments were determined according to approved IACUC protocols. Sample size selection was based on previous studies that allow for detection of meaningful differences or associations. Randomization was not applied, as the study involved untreated mice without intervention groups. All animals were maintained under standardized conditions, including controlled housing, diet, and environmental

factors, to minimize variability. Blinding was not performed for the in vivo experiments.

Light-sheet microscopy

Mice carrying KP4-mCherry and HPAC-eGFP derived tumours were anaesthetized by intraperitoneal ketamine/xylazine injection and then perfused through the inferior vena cava with 10 ml of PBS and 10 ml of 1% PFA in PBS, allowing outflow through the portal vein. For fixation, lungs were inflated with 1% PFA prior to excision and stored overnight. Samples were cleared using the CUBIC protocol as previously described^{60,61} and stained with AlexaFluor 594-conjugated antibody against mCherry (clone 16D7; Invitrogen, 74-000-3TP594; 1:100), AlexaFluor 647-conjugated antibody against GFP (rabbit polyclonal; Invitrogen, A-31852; 1:100), and Cy3-conjugated antibody against α-smooth muscle actin (clone 1A4; Sigma-Aldrich, C6198; 1:250). Cleared samples were imaged using the UltraMicroscope Blaze (Miltenyi Biotec) light-sheet microscope with a 1.0× objective and z-step size of 5 μm. For three-dimensional image analysis, Imaris software (Bitplane, v10.0.0) and Imaris Stitcher were used to process and stitch the images. Individual mCherry⁺ and eGFP⁺ cells were identified and quantified using the Imaris Surface tool.

Mouse hepatocyte isolation and culture

Hepatocyte isolation was performed as previously described⁶². In brief, C57BL/6 mice were anaesthetized, and midline laparotomy was performed to expose the liver. The vena cava was cannulated with a 27-gauge needle connected to a perfusion system. The liver was perfused sequentially with chelation buffer (EDTA-containing) to remove blood and calcium ions, followed by digestion buffer (containing liberase) to disrupt tissue structure and release hepatocytes. The liver sac was carefully opened, and the perfusate containing dissociated hepatocytes was collected in a sterile container. The collected solution was centrifuged to pellet the hepatocytes. The pellet was then resuspended in a Percoll solution and layered onto a Percoll density gradient. Centrifugation was performed to separate living hepatocytes from debris and non-parenchymal cells. Purified hepatocytes were resuspended in plating media (DMEM low glucose supplemented with 5% FBS and 1% penicillin-streptomycin) and seeded onto culture plates coated with 0.1 μg ml⁻¹ of collagen (Corning, 354236). Cells were incubated at 37 °C with 5% CO₂ for 3 h to allow initial attachment, after which plating media was replaced with maintenance media (Williams E media supplemented with 2 mM L-glutamine and 1% penicillin-streptomycin) overnight. Hepatocytes were then treated with conditioned media obtained from human PDAC cell lines as outlined in the figures. To rescue the CYP46A1-knockout effect, 24-hydroxycholesterol (Sigma, SML-1648) was used at a concentration of 25 μM for the duration of the experiment (24 h).

Human samples

Archival de-identified sections of unmatched human primary, liver metastases and lung metastases specimens were obtained from UCSF Pathology. Human PDAC specimens were selected under Institutional Review Board (IRB)-approved protocol 18-25787. PDAC patients with isolated lung metastases (M1-PUL cohort, n = 10) were retrospectively identified at the Ludwig-Maximilians-University of Munich, Germany, by analysing medical records and correlating computed tomography (CT). The occurrence of M1-PUL was confirmed by histology or retrospective review of serial CT scans, which showed enlarging pulmonary nodules over time. To rule out synchronous extrapulmonary dissemination, abdominal CT scans were reviewed for the presence of extrapulmonary metastases. PDAC patients with isolated liver metastases (M1-LIV cohort, n = 10) were used as a control cohort from the Ludwig-Maximilians-University of Munich, Germany. These patients were clinic-pathologically matched, as described previously⁶³. Formalin-fixed paraffin-embedded blocks of these primary tumours

Article

were collected, as were patient and tumour characteristics, including age, sex, tumour-node-metastasis (TNM) stage, grading and medical information about diabetes, smoking, hypercholesterolemia, and statin usage. Project approval was granted by the ethics committee at Ludwig-Maximilians-University of Munich, Germany (approval number 134-15,20-1085, and 284-10). The H&E-stained sections of human lesions were examined in a blinded manner by pathologists to assess tissue morphology, cellular characteristics, and tumour features such as differentiation.

MetMap analysis of PDAC cell line metastatic potential and penetrance

Data corresponding to MetMap500 was downloaded from <https://www.depmap.org/metmap/vis-app/index.html>. MetMap500 provides both the metastatic potential (expressed as \log_{10} mean value ranging from -4 to 4) and metastatic penetrance (expressed as a value between 0 and 1) for 498 human cancer cell lines following intracardiac injection and subsequent seeding in 5 metastatic organs (kidney, bone, lungs, brain, or liver). For each metastatic organ site the 'mean' values corresponding to the 30 PDAC cell lines used in the study was transformed to the original data. The relative metastatic potential (Met^{pot}) and penetrance (Met^{pen}) for each organ was calculated using the formula

$$\text{Relative}_P = \frac{P_{\text{organ}}}{\sum_5 P_{\text{organs}}}$$

where P is either penetrance or potential, 'organ' refers to either kidney, bone, lungs, brain or liver and 'organs' refers to all organs combined. Cell lines with the same potential for each organ were excluded ($n = 5$ cell lines). Data are graphically represented as petal plots with the length being the relative potential and colour indicating penetrance.

Principal component analysis

Principal component analysis was conducted using the fvizcluster function from the factoextra package in R version.3.1093 along with the pca_transform function from the same package to explore the underlying structure of the metastatic potential and penetrance of the 25 PDAC cell lines. This analysis utilized the five organ Met^{pen} and five organ Met^{pot} values for each PDAC cell line. Scatter plots of the second and third principal components were generated, with points coloured according to sample groups or conditions. Petal plots were generated using the values generated to form the principal component analysis. Graphical representation was derived using GGPlot2 in R version.3.1093.

GSEA

Gene Set Enrichment Analysis (GSEA) was performed to compare the liver and lung clusters of cell lines using gene sets derived from the signatures from Adams et al.⁶⁴ and Moffit et al.²¹. The analysis was conducted using version 4.1.0 of the GSEA software. Expression data for all cell lines within the liver and lung clusters were collected and pre-processed. The gene expression profiles were normalized and log-transformed to ensure comparability across samples. Enrichment scores were calculated for each gene set, indicating the degree of enrichment in the liver cluster compared to the lung cluster, and vice versa. Statistical significance of the enrichment scores was assessed using the GSEA software.

Correlation between liver:lung ratio and classical score

A scatter plot was generated to visualize the relationship between the liver:lung ratio and classical score derived from Adams et al.⁶⁴ and Moffit et al.²¹ for each cell line. The liver:lung ratio was calculated by dividing the liver metastatic potential by the lung metastatic potential for each PDAC cell line according to the formula

$$\text{Liver : lung ratio} = \log_2 \frac{\text{relative liver metastatic potential}}{\text{relative lung metastatic potential}}$$

For the calculation of the classical score, we compiled all genes included in the classical gene signature used in Adams et al.⁶⁴ and Moffit et al.²¹. Using gene expression data extracted from the MetMap dataset, a z-score was computed for each classical signature associated gene for all PDAC cell lines. Aggregate z-scores were then compiled, yielding a classical score for each PDAC cell line. Pearson correlation coefficient (R) and P value were calculated to assess the relationship between the liver:lung ratio and classical score.

Gene expression correlation analysis

The DepMap RNA-sequencing expression dataset was used to determine the top correlated genes associated with classical genes (*GATA6*, *S100P*, *FOXQ1* and *CDH1*) and basal genes (*VIM* and *ZEB1*). Pearson correlation values for positively and negatively associated genes were plotted against gene rank. Red points on the scatter plot correspond to statistically significant correlations. The relative correlation of the above classical and basal genes with *PCSK9* was also determined using DepMap RNA-sequencing expression data. The Pearson correlation coefficient (R) and P value for each correlation was calculated to assess the linear relationship between the two variables.

Single-cell RNA-sequencing analysis

Datasets were uploaded from Zhang et al.²⁷ and analysed as follows. Cells with nFeature_RNA less than 200 and the percentage of mitochondrial reads being more than 20% were filtered out from the single-cell RNA-sequencing datasets using the Seurat package (version 4.3.0)⁶⁵. DoubletFinder package (version 2.0.4)⁶⁶ was applied to find doublet cells and filter them out. Filtered data were then log normalized, scaled and integrated. The sctransform (SCT) assay was used to do the clustering on each sample and the integrated dataset. Cell annotation was carried out using the SingleR⁶⁷ and the vamForSeurat function incorporating some known marker genes. InferCNV package (version 1.14.2)⁶⁸ was implemented on each sample to identify malignant cells, designating immune cells as the reference group. On the basis of the inferCNV results, copy number variation (CNV) score and CNV correlation were calculated. Cells exhibiting a CNV score greater than 0.015 and a CNV correlation exceeding 0.4 were identified as malignant cells while those with scores below these thresholds were identified as non-malignant cells. On the basis of the cell type annotation and identified malignant cells, the RNA expression of *PCSK9* was compared among different cell groups.

To compare the expression of *PCSK9* in basal and classical subtypes within malignant cells, cells were re-clustered using the ReclusterCells function from the SCISSORS package⁶⁹. The following parameter settings were applied: use.sct = TRUE, n.HVG = 3000, n.PC = 20, resolution, vals = c(0.05, 0.1, 0.2, 0.3, 0.4), k.vals = c(10, 20, 30, 40), with other parameters using default values. The basal and classical subclusters were identified based on the variance-adjusted mahalanobis (VAM) score, calculated using the function vamForSeurat from the VAM package. Previously published basal and classical subtype signature genes^{21,69} were used for this analysis. The clusters with higher basal VAM scores and lower classical VAM scores were annotated as basal, while those with higher classical VAM scores and lower basal VAM scores were annotated as classical. A comparative analysis of *PCSK9* gene expression was subsequently conducted between the basal and classical subtypes.

Image processing and analysis

To measure fluorescence intensity and colocalization, images were analyzed using Fiji software. This allowed for precise quantification of fluorescence signals and determination of colocalized areas within the images. Images acquired for analysis underwent processing utilizing Fiji software plug-ins. For crystal violet proliferation quantification, the plugin ReadPlate was employed. Fiji with automated counting was used to quantify the number of colonies present in each well.

Statistical analysis and reproducibility

Statistical analysis was conducted to assess the significance of observed differences between experimental groups. For comparisons between two groups, a two-tailed *t*-test was employed, utilizing Prism 8 software. For experiments involving more than two groups, one-way ANOVA was utilized. Post hoc analysis was performed to compare individual groups following ANOVA. Specifically, the Bonferroni post hoc test was employed in all cases except *in vivo* experiments where the least significant difference post hoc test was utilized to adjust for multiple comparisons. All statistical analyses were performed using standard statistical software packages. Statistical significance was defined as $P < 0.05$. Pearson correlations were performed using the ggpqr package (version 0.6.0), the stat_cor function with ‘pearson’ method.

All experiments were performed with appropriate biological replicates. Each immunoblot was independently repeated at least three times with similar results to ensure reproducibility. Sample sizes, statistical analyses and specific tests used are detailed in the methods section and figure legends. No data points were excluded, and blinding or randomization was applied where applicable. Statistical tests were not used to predetermine sample size.

Reporting summary

Further information on research design is available in the Nature Portfolio Reporting Summary linked to this article.

Data availability

Metabolomics data including 7-DHC and 7-DHD quantification were deposited on the Metabolomics Workbench platform at <http://dx.doi.org/10.21228/M8RV70> (project ID: PRO02405)⁷⁰. Single-cell RNA-sequencing data are available from ref. 27. Additional resources from the Cancer Research Training Program (CRTP) can be found at <https://crtcp.ccr.cancer.gov/>.

59. Liang, X. et al. Rapid and highly efficient mammalian cell engineering via Cas9 protein transfection. *J. Biotechnol.* **208**, 44–53 (2015).
60. Susaki, E. A. et al. Advanced CUBIC protocols for whole-brain and whole-body clearing and imaging. *Nat. Protoc.* **10**, 1709–1727 (2015).
61. Tainaka, K. et al. Whole-body imaging with single-cell resolution by tissue decolorization. *Cell* **159**, 911–924 (2014).
62. Charni-Natan, M. & Goldstein, I. Protocol for primary mouse hepatocyte isolation. *STAR Protoc.* **1**, 100086 (2020).

63. Guenther, M. et al. The impact of adjuvant therapy on outcome in UICC stage I pancreatic cancer. *Int. J. Cancer* **151**, 914–919 (2022).
64. Adams, C. R. et al. Transcriptional control of subtype switching ensures adaptation and growth of pancreatic cancer. *eLife* **8**, e45313 (2019).
65. McGinnis, C. S., Murrow, L. M. & Gartner, Z. J. DoubletFinder: doublet detection in single-cell RNA sequencing data using artificial nearest neighbors. *Cell Syst.* **8**, 329–337 e324 (2019).
66. Aran, D. et al. Reference-based analysis of lung single-cell sequencing reveals a transitional profibrotic macrophage. *Nat. Immunol.* **20**, 163–172 (2019).
67. Tirosh, I. et al. Dissecting the multicellular ecosystem of metastatic melanoma by single-cell RNA-seq. *Science* **352**, 189–196 (2016).
68. Zhang, L. et al. Single-cell analyses inform mechanisms of myeloid-targeted therapies in colon cancer. *Cell* **181**, 442–459.e429 (2020).
69. Leary, J. R. et al. Sub-cluster identification through semi-supervised optimization of rare-cell silhouettes (SCISSORS) in single-cell RNA-sequencing. *Bioinformatics* **39**, btad449 (2023).
70. Rademaker, G. Summary of project PRO02405. *Metabolomics Workbench* <http://dx.doi.org/10.21228/M8RV70> (2025).

Acknowledgements This work was supported by a BAEF (Belgian American Education Foundation) fellowship, Fonds Léon Fredericq, Rotary and Wallonie Bruxelles International grants (G.R.); a National Science Foundation Graduate Research Fellowship (NSF2034836) (G.A.H.); NHLBI R35 HL161241 and the Nina Ireland Program for Lung Health (M.R.L.); National Cancer Institute RO1CA260205 (R.Z.); National Cancer Institute RO1CA240603 and RO1CA260249, the Ed Marra Passion to Win Fund, the Weston Havens Fund and the AACR-MPM Transformative Cancer Research Award (R.M.P.); National Cancer Institute RO1CA199064 (J.J.Y.), U01CA274298, P50CA257911 and U24CA211000 (X.L.P. and J.J.Y.); 7R01CA260860 and 7R01CA256969 (E.A.C.); Sky Foundation fellowship (L.M.P.); and National Institute of Diabetes and Digestive and Kidney Diseases R01DK131227 and P30DK026743 (B.W.). The authors thank the UCSF Parnassus Flow CoLab, RRID:SCR_018206 for assistance with flow cytometry and the UCSF Liver Center, supported by P30DK026743, for assistance with hepatocyte isolation.

Author contributions G.R. conceived the project, performed most experiments and wrote the manuscript. G.A.H. conducted tail vein and intracardiac injections and assisted with experiments. Y.S. performed the light-sheet imaging experiment. S.D. performed immunoblotting and RT-qPCR analyses. L.M.-P., S.F.K., S.B., S.O., M.G., V.H. and M.H. accrued and provided the matched PDAC primary patient specimens. A.L.L. cloned the PCSK9 plasmids and variants. X.L.P. and C.L. performed analysis of single-cell RNA-sequencing data. L.Q. performed the intrasplenic injections. M.A.L. performed flow cytometry and data analysis. K.W.W. and G.E.K. contributed PDAC specimens and performed blinded analysis. B.W., E.A.C., M.R.L., J.J.Y. and R.Z. supervised the research and provided intellectual feedback. R.M.P. conceived the project, supervised the research, wrote and edited the manuscript.

Competing interests The authors declare no competing interests.

Additional information

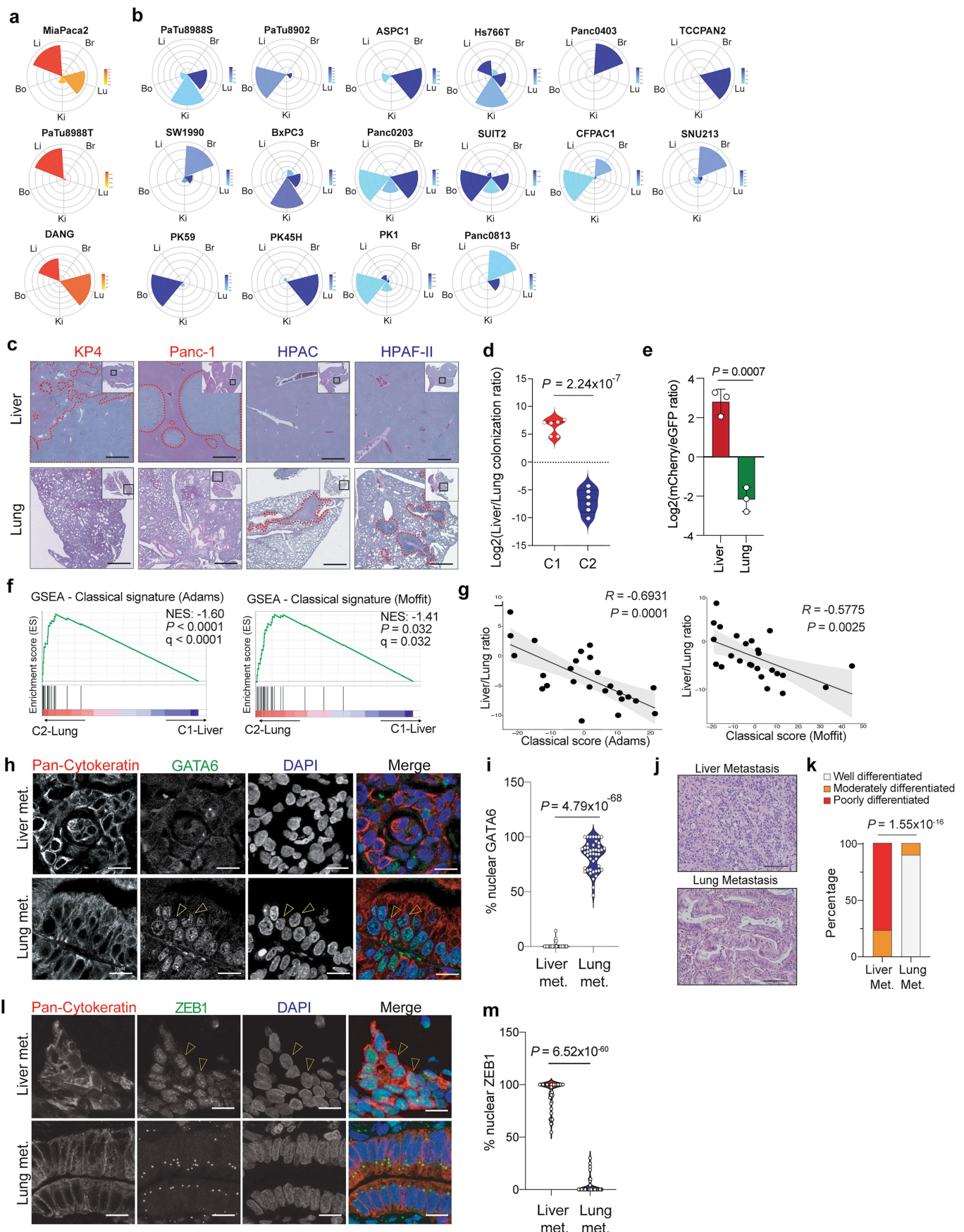
Supplementary information The online version contains supplementary material available at <https://doi.org/10.1038/s41586-025-09017-8>.

Correspondence and requests for materials should be addressed to Rushika M. Perera.

Peer review information *Nature* thanks the anonymous reviewer(s) for their contribution to the peer review of this work.

Reprints and permissions information is available at <http://www.nature.com/reprints>.

Article



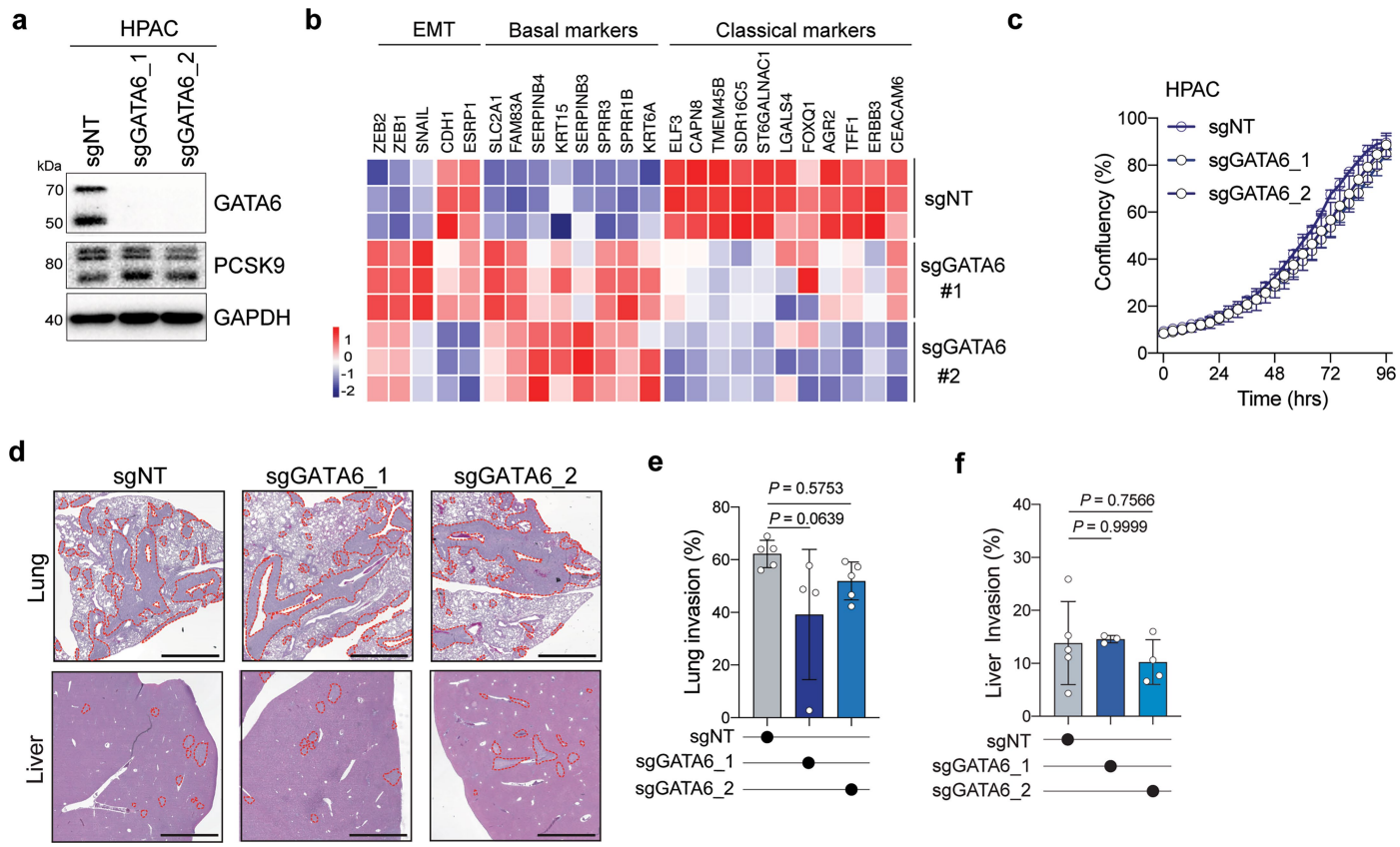
Extended Data Fig. 1 | See next page for caption.

Extended Data Fig. 1 | Liver- and Lung-avid cell lines exhibit distinct features.

a, b. Petal plots depicting metastatic potential (length) and penetrance (width) for C1-Liver lines (a) and C2-Lung lines (b), extracted from the MetMap 500 analysis. Br, Brain; Bo, Bone; Ki, Kidney; Li, Liver; Lu, Lung. **c.** Representative H&E images showing tumor growth (red outline) in the liver (top) and lung (bottom) 3 weeks post intra-cardiac injection of the indicated PDAC cell lines. Scale bars: 500 μ m. **d.** Quantification of liver/lung colonization ratio of C1-Liver and C2-lung lines for the experiment in c. (n = 6 mice per/cluster). Statistical significance was calculated using a two-tailed t-test. **e.** Flow cytometry-based measurement of relative eGFP or mCherry enrichment in the liver or lungs. mCherry positive cells were more abundant in the liver while eGFP positive cells were more abundant in the lungs (related to Fig. 1l–n). Statistical significance was calculated using a two-tailed t-test. Error bars depict standard deviation. (n = 3 tissues per condition). **f.** Gene set enrichment analysis (GSEA) plots showing relative enrichment of the PDAC classical gene signature derived from Adams et al. and Moffit et al. in cluster 1 (C1-Liver) and cluster 2 (C2-Lung) cell lines. Statistical significance was calculated using a permutation test with FDR adjustment. **g.** Scatter plot showing correlation between liver/lung metastatic potential ratio (see Supplementary Table 2) and classical score from Adams

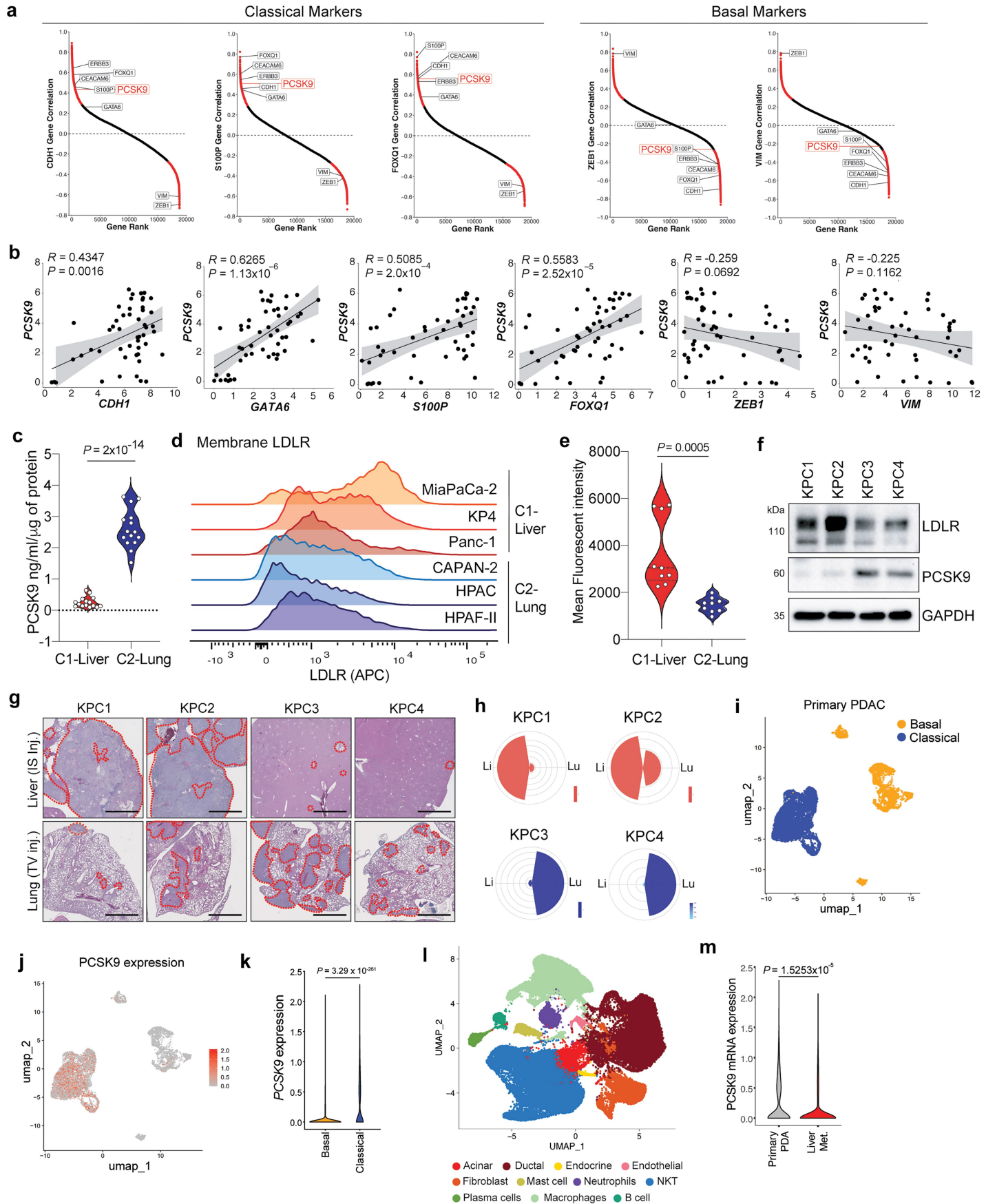
et al. and Moffit et al. Each dot represents a PDAC cell line (n = 25). Linear regression followed by Pearson correlation. Error margins (grey) depict standard error of the mean. **h.** Representative immunofluorescence images of GATA6 (green), Pan-Cytokeratin (CK19) (red), DAPI (blue) in liver (top) and lung (bottom) patient PDAC metastases. Note the nuclear localization of GATA6 in lung metastases. Scale bars: 20 μ m. **i.** Quantification of the percentage nuclear GATA6 in liver (56 fields from n = 3 samples) and lung (45 fields from n = 3 samples) metastases sections. Statistical significance was calculated using a two tail T-test. **j.** Representative H&E images of human liver and lung PDAC metastases. Scale bar: 20 μ m. **k.** Bar plot depicting quantification of the differentiation status of PDAC liver and lung metastases shown in j. (Liver metastases n = 45; Lung metastases n = 10). Statistical significance was calculated using a two-tailed t-test. **l.** Representative immunofluorescence images of ZEB1 (green), Pan-Cytokeratin (CK19) (red), DAPI (blue) in liver and lung patient PDAC metastatic lesions. Note the nuclear localization of ZEB1 in the liver metastases. Scale bars: 20 μ m. **m.** Quantification of the percentage nuclear ZEB1 in liver (55 fields from n = 5 samples) and lung (40 fields from n = 5 samples) metastases sections. Statistical significance was calculated using a two tail T-test. For flow cytometry source data, see Supplementary Fig. 2.

Article



Extended Data Fig. 2 | Basal/classical PDAC subtypes do not impact metastatic organ preference. **a.** Immunoblot of the indicated proteins following CRISPR mediated knockout of GATA6 in HPAC cells. **b.** Heatmap depicting normalized mRNA expression of the indicated genes, measured by qRT-PCR in HPAC cells with or without GATA6 knockout. **c.** In vitro proliferation rate of the cells shown in a. ($n = 3$ replicates per group). **d.** Representative H&E images of lung (top), and liver (bottom) 4 weeks post tail-vein or intrasplenic injection, respectively, of HPAC cells following GATA6 knockout. Scale Bar: 1 mm.

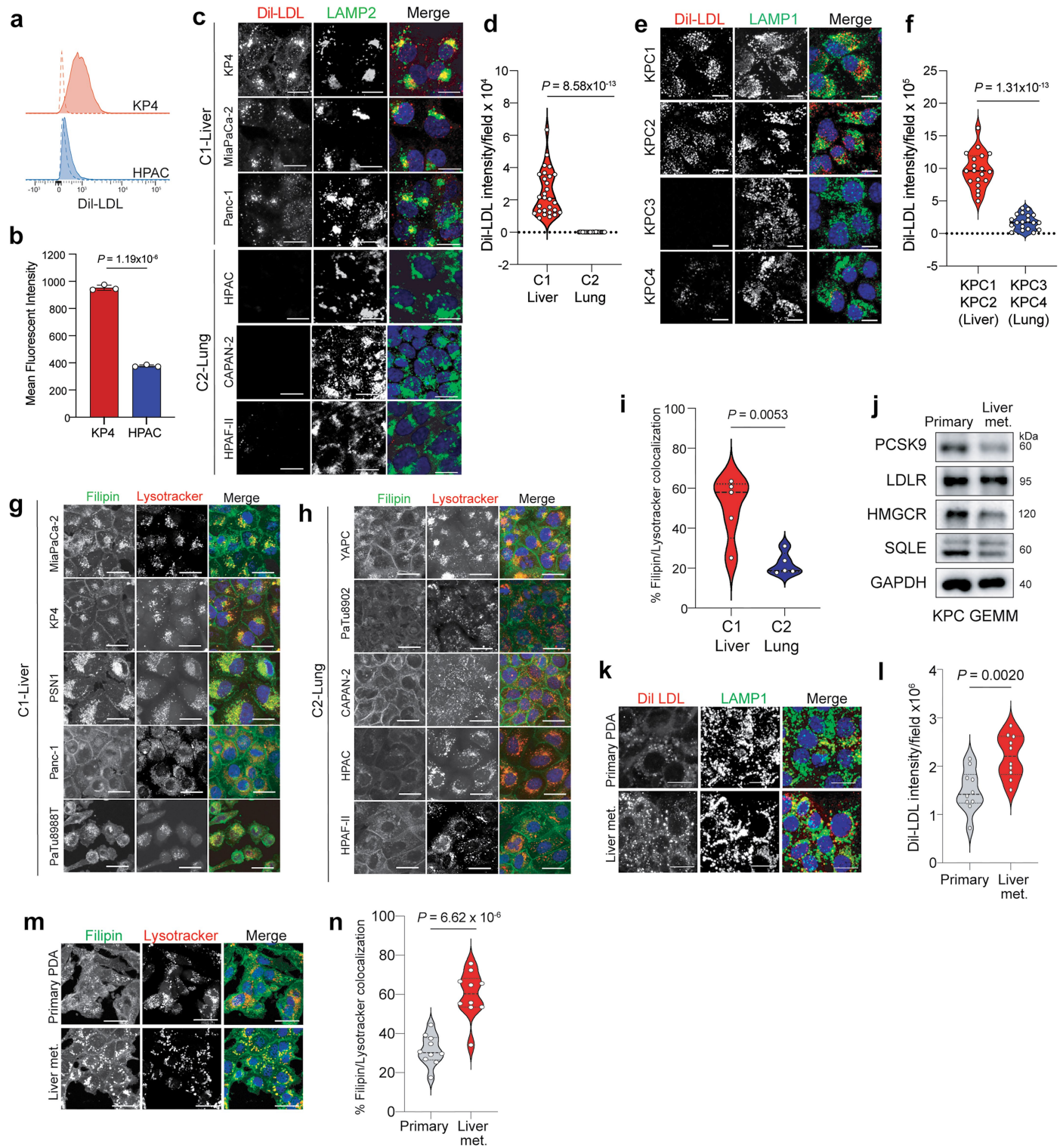
e. Percentage tumour area in the lungs from samples shown in d. Statistical significance was calculated using a one-way ANOVA with Bonferroni correction. sgNT: $n = 5$; sgGATA6_1: $n = 4$; sgGATA6_2: $n = 5$. **f.** Percentage tumour area in the liver from samples shown in d. Statistical significance was calculated using a one-way ANOVA with Bonferroni correction. sgNT: $n = 5$; sgGATA6_1: $n = 3$; sgGATA6_2: $n = 4$. All error bars represent standard deviation of the mean. For gel source data, see Supplementary Fig. 1.



Extended Data Fig. 3 | See next page for caption.

Article

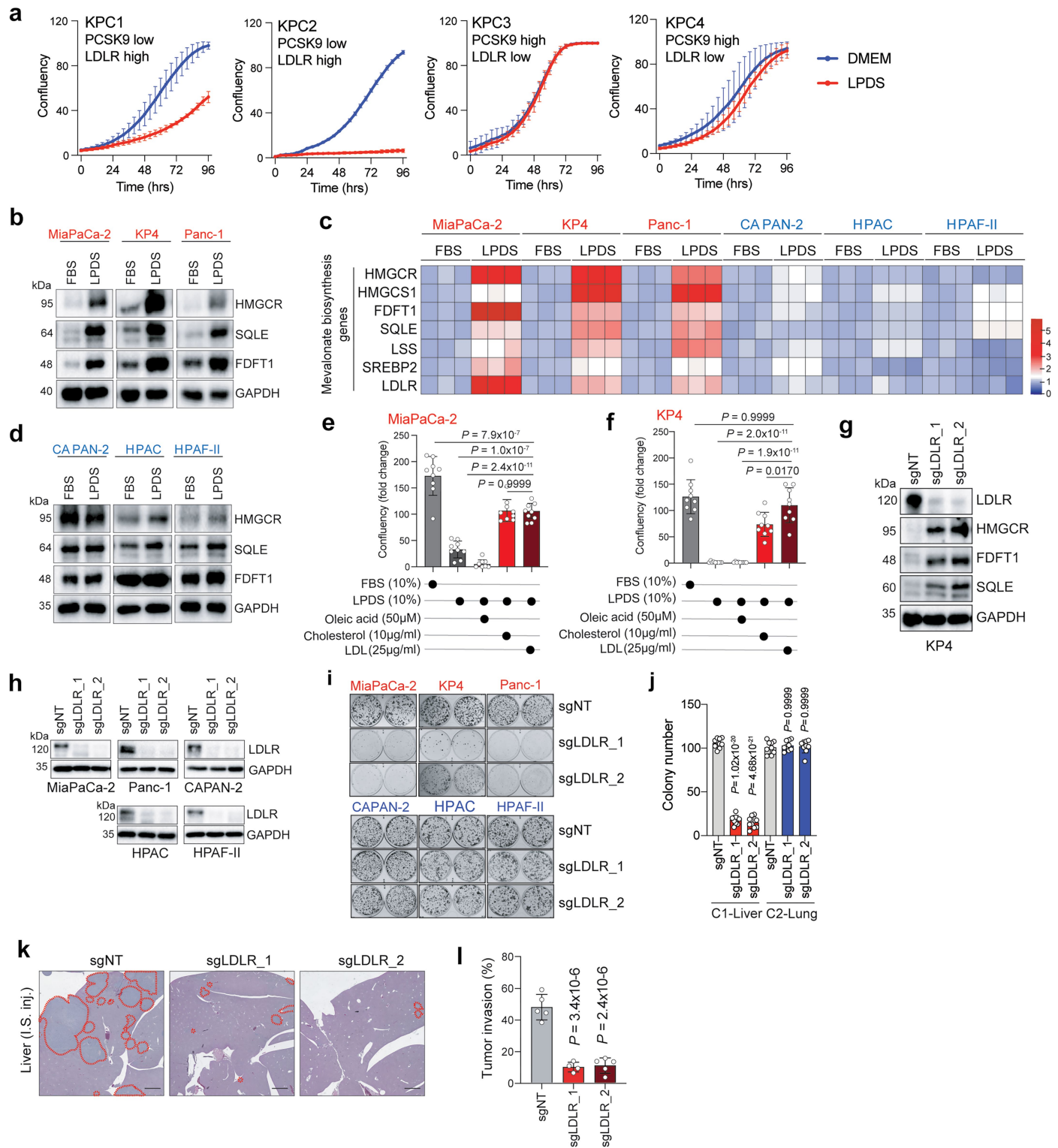
Extended Data Fig. 3 | High PCSK9 expression is correlated with classical PDAC subtype and lung colonization. **a.** Gene expression correlation of PCSK9 relative to the indicated classical (*CDH1*, *S100P*, *FOXQ1*) and basal (*VIM*, *ZEB1*) genes across all PDAC cell lines available on DepMap. Statistically significant correlations are indicated in red, and non-significant correlations are indicated in black. Gene rank for the indicated genes are shown in each plot. **b.** Scatter plot showing expression correlation between PCSK9 and individual classical (*CDH1*, *GATA6*, *S100P*, *FOXQ1*) and basal (*ZEB1*, *VIM*) genes (data extracted from $n = 50$ cell lines available in DepMap). Linear regression followed by Pearson correlation. Error margins (grey) depict standard error of the mean. **c.** ELISA based quantification of secreted PCSK9 protein from conditioned media collected from C1-Liver ($n = 5$) and C2-Lung ($n = 5$) cell lines. Dots represent $n = 3$ biological replicates per cell line. Statistical significance was calculated using a two tail T-test. **d.** Representative flow cytometry-based detection of plasma membrane LDLR in C1-Liver ($n = 3$) and C2-Lung ($n = 3$) cell lines. **e.** Quantification of the mean fluorescent intensity of plasma membrane LDLR from the cell lines in d. ($n = 3$ biological replicates per cell line). Statistical significance was calculated using a two tail T-test. **f.** Immunoblot of the indicated proteins in mouse derived KPC cell lines. **g.** Representative H&E images of tumor burden in the liver (top) and lung (bottom) 2 weeks post intrasplenic or tail-vein injection, respectively, of the indicated KPC cell lines. ($n = 3$ mice/cell line). Scale Bar: 500 μ m. **h.** Petal plots depicting metastatic potential (length) and penetrance (colour) for the indicated cell lines based on data generated in g. Li, Liver; Lu, Lung. **i.** UMAP plot of single cell sequencing from $n = 3$ primary PDAC lesions depicting two clusters representing the classical (blue) and basal (yellow) subtypes in ductal cells. **j.** UMAP plot showing enrichment of PCSK9 mRNA expression in the classical PDAC subtype as depicted in i. **k.** Quantification of PCSK9 mRNA expression in ductal cells corresponding to basal and classical PDAC subtypes. Statistical significance was calculated using a two-tailed t-test. **l.** UMAP plot of single cell sequencing from $n = 3$ primary PDAC and $n = 4$ matched liver metastases. Colors represent different cell types. **m.** PCSK9 mRNA expression in ductal cells from primary PDAC and liver metastases. Statistical significance was calculated using a two-tailed t-test. For gel source data, see Supplementary Fig. 1.



Extended Data Fig. 4 | See next page for caption.

Article

Extended Data Fig. 4 | Liver-avid cells uptake LDL cholesterol. **a,b.** Flow cytometry plots of plasma membrane Dil-LDL in KP4 and HPAC cell lines (a). The dotted line depicts the negative control staining. Graph depicts quantification of data (b). Data points represent the average of 3 technical replicates from $n = 3$ biological replicates. Error bars represent standard deviation. **c,d.** Representative immunofluorescence images (c) and quantification (d) of Dil-LDL uptake (red) in C1-Liver and C2-Lung lines. Cells are co-stained for LAMP2 (green) and DAPI (blue). Scale bars: 10 μm . ($n = 10$ fields/cell line). **e,f.** Representative immunofluorescence images (e) and quantification (f) of Dil-LDL uptake (red) in four mouse KPC derived cell lines. Note that KPC1 and KPC2 take up exogenous LDL while KPC3 and KPC4 do not. Cells are co-stained for LAMP1 (green) and DAPI (blue). Scale bars: 10 μm . ($n = 10$ fields/cell line). **g-i.** Representative immunofluorescence images depicting Filipin (green) in C1-Liver (g), C2-Lung (h) lines and quantification (i). Cells are co-stained for Lysotracker (red) and DAPI (blue). Scale bars: 10 μm . Data points represent the average of at least 7 fields from $n = 5$ cell lines/group. **j.** Immunoblot for the indicated proteins in KPC derived cells isolated from isogenic primary tumor and liver metastases. **k,l.** Representative immunofluorescence images (k) and quantification (l) of Dil-LDL uptake (red) in the KPC lines in j. Cells are co-stained for LAMP1 (green) and DAPI (blue). Scale bars: 10 μm . ($n = 10$ fields/cell line). **m,n.** Representative immunofluorescence images (m) and quantification (n) of Filipin (green) in the KPC lines in j and k. Cells are co-stained for Lysotracker (red) and DAPI (blue). ($n = 10$ fields/cell line). Scale bars: 10 μm . Statistical significance was calculated using a two-tailed t -test for data shown in b, d, i, l, and n. For gel source data, see Supplementary Fig. 1. For flow cytometry source data, see Supplementary Fig. 2.

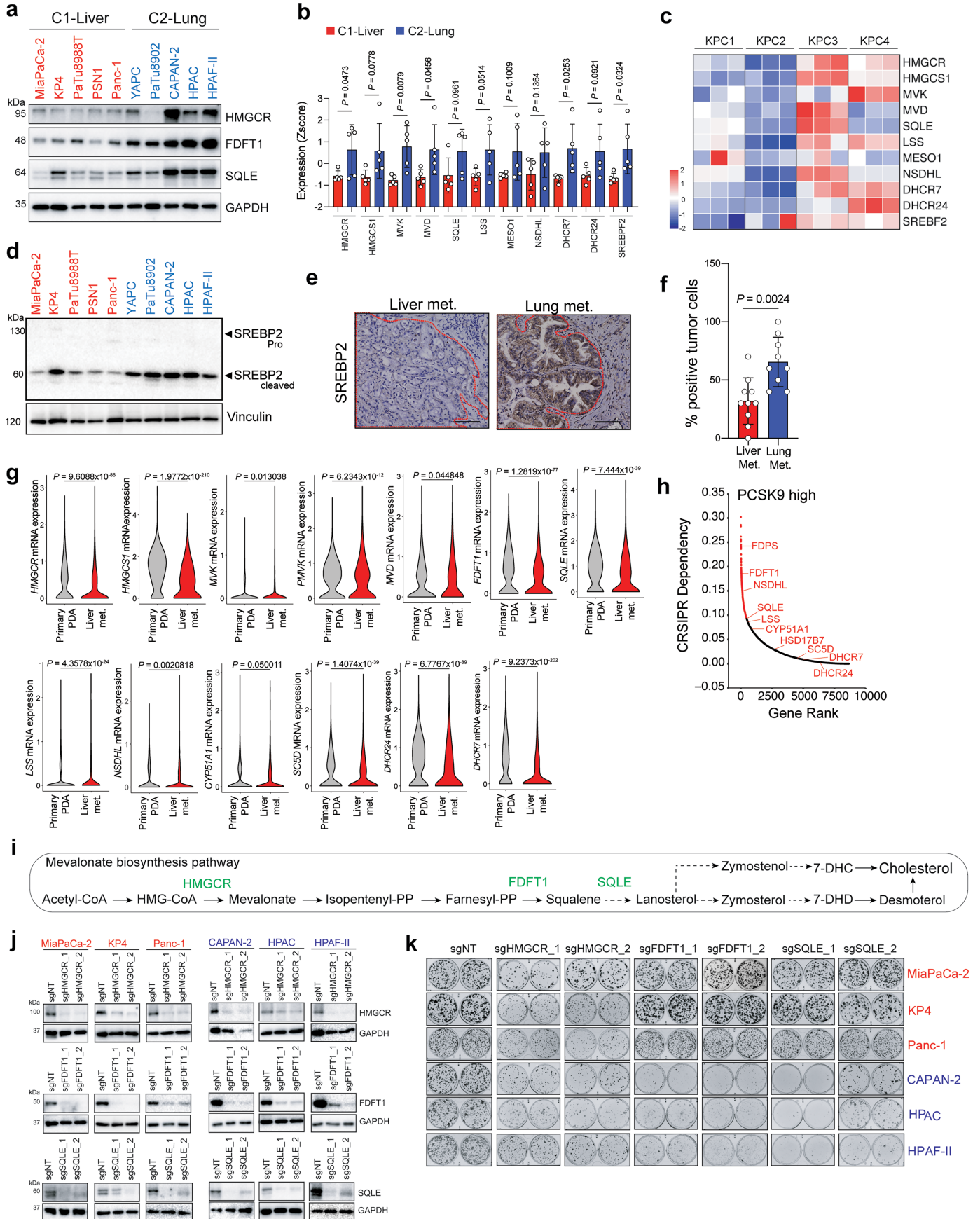


Extended Data Fig. 5 | See next page for caption.

Article

Extended Data Fig. 5 | Liver-avid cells rely on LDL-cholesterol uptake for growth. **a.** Growth curves of KPC lines cultured in DMEM with FBS or LPDS. (n = 3 replicates per condition). **b.** Immunoblot of the indicated proteins in C1-Liver lines following treatment with DMEM containing FBS or LPDS for 72 h. **c.** Heatmap depicting the expression levels of mevalonate pathway genes in C1-Liver and C2-Lung lines. Each row represents a specific gene and columns represent biological replicates for each cell line. Expression levels are expressed as z-scores. **d.** Immunoblot of the indicated proteins in C2-Lung lines following treatment with DMEM containing FBS or LPDS for 72 h. **e,f.** Relative cell confluence of MiaPaCa2 (e) and KP4 (f) cells cultured in the indicated media supplemented with cholesterol, LDL or oleic acid. Statistical significance is calculated using a one-way ANOVA with Bonferroni correction. (n = 9 biological replicates per conditions). **g,h.** Immunoblots of the indicated proteins in KP4

cells (g) and additional cell lines (h) following CRISPR mediated knockout of LDLR. **i.** Representative images of colony forming assays of C1-Liver lines and C2-Lung lines following CRISPR mediated knockout of LDLR. **j.** Quantification of colony forming number from images in i. Statistical significance was calculated using a one-way ANOVA with Bonferroni correction. (n = 9 biological replicates/condition). **k.** Representative H&E images showing tumor growth (red outline) in the liver 4 weeks post intra-splenic injection of KP4 cells expressing control sgRNA or LDLR targeting sgRNA. Scale bars: 1 mm. **l.** Quantification of tumor area from data in g. Statistical significance was calculated using a one-way ANOVA with Bonferroni correction. sgNT: n = 5 mice; sgLDLR_1: n = 4 mice; sgLDLR_2: n = 5 mice. All error bars represent standard deviation of the mean. For gel source data, see Supplementary Fig. 1.



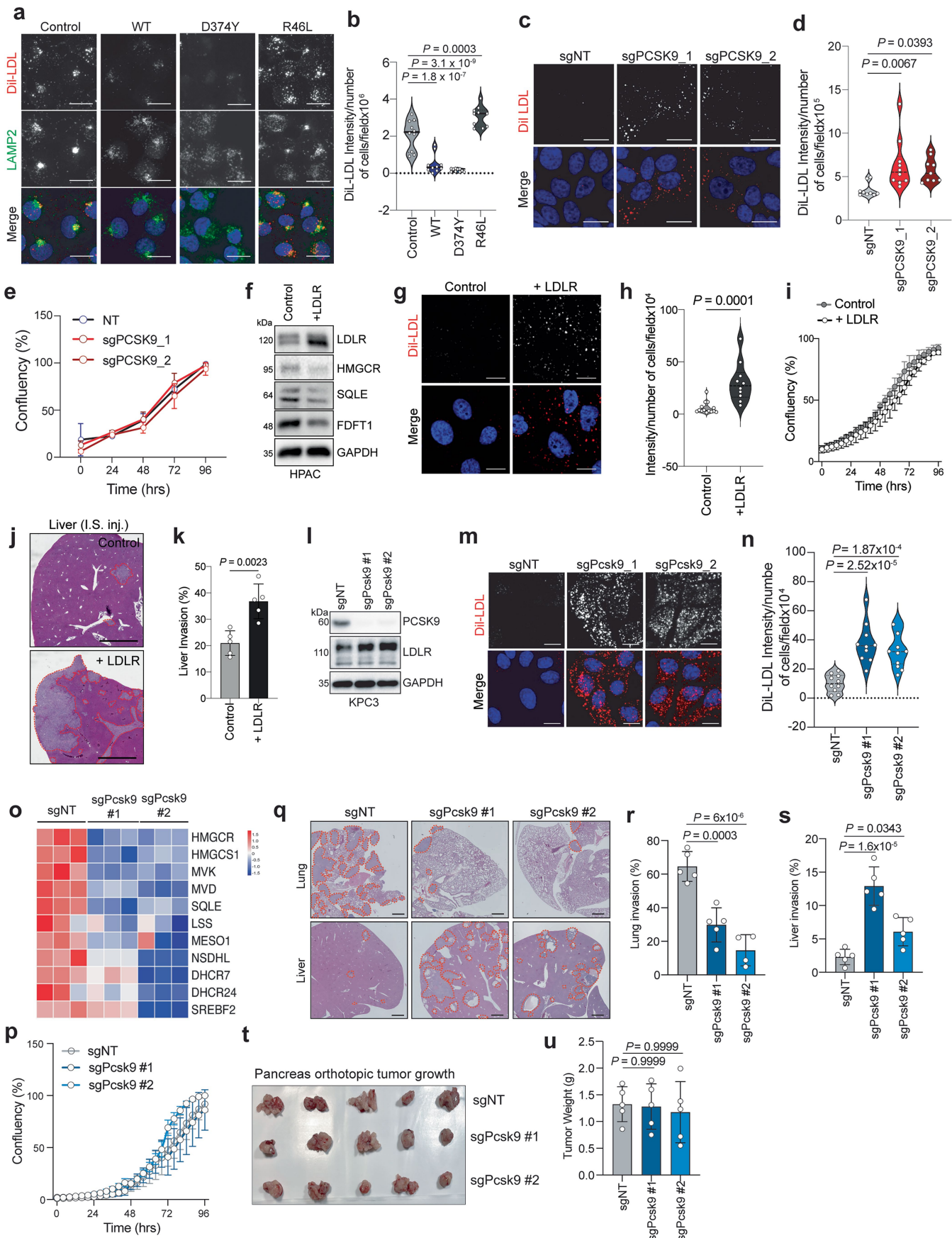
Extended Data Fig. 6 | See next page for caption.

Article

Extended Data Fig. 6 | Lung-avid cells rely on cholesterol biosynthesis.

a. Immunoblot of the indicated proteins in C1-Liver and C2-Lung lines.
b. Quantitative real-time PCR measurement of the indicated genes in C1-Liver ($n = 5$) and C2-Lung ($n = 5$) lines expressed as z-score. Each point represents the average of $n = 3$ biological replicates for each line. Statistical significance was calculated using a two-tailed t-test.
c. Heatmap depicting mRNA expression of the indicated genes measured by qRT-PCR displayed as z-score. ($n = 3$ biological replicates per line).
d. Immunoblot for SREBP2 in the indicated cell lines.
e. Representative immunohistochemistry images of SREBP2 in liver (left) and lung (right) metastases. Scale bar = 100 μm .
f. Quantification of SREBP2 staining intensity from $n = 10$ liver and $n = 9$ lung metastases depicted in e. Statistical significance was calculated using a two tailed t-test.
g. Expression

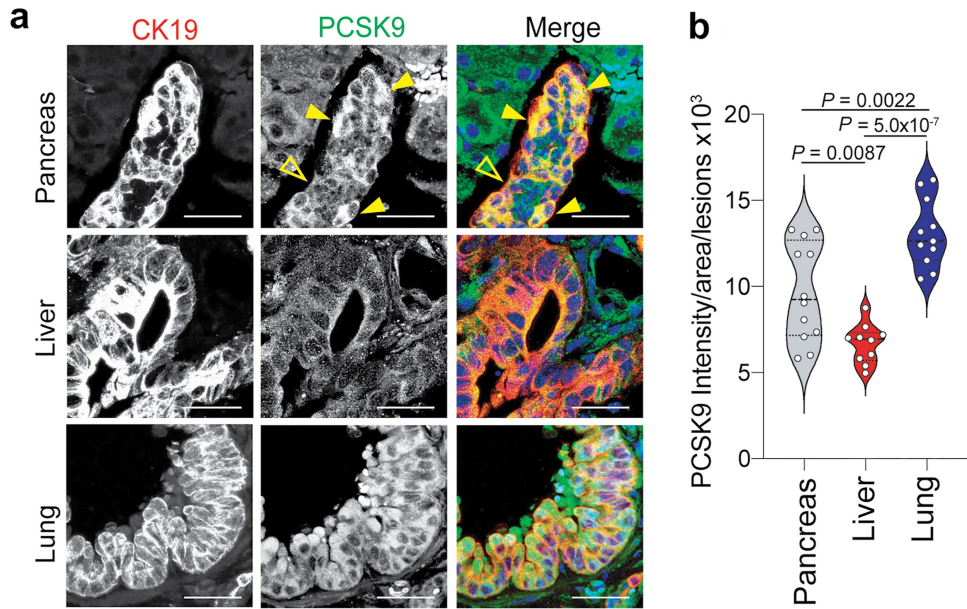
levels of cholesterol biosynthesis genes in single cell RNA sequencing data from primary PDAC ($n = 3$) and the matched liver metastases ($n = 4$). Statistical significance was calculated using a two-tailed t-test.
h. DepMap CRISPR dependency ranking of top genes associated with PCSK9 high status across PDAC. Cholesterol biosynthesis genes are indicated. Red dots indicate significant genes and black dots indicate non-significant genes.
i. Reactions of the cholesterol biosynthesis pathway with key enzymes highlighted in green.
j. Immunoblot for the indicated proteins following CRISPR mediated knockout of the indicated genes (related to data presented in fig. 3c,d).
k. Representative images of colony forming assays of C1-Liver and C2-Lung lines upon CRISPR-mediated knockout of the indicated genes. All error bars represent standard deviation of the mean. For gel source data, see Supplementary Fig. 1.



Extended Data Fig. 7 | See next page for caption.

Article

Extended Data Fig. 7 | Altering PCSK9-LDLR status leads to a switch in cholesterol metabolism and metastatic organ preference. **a.** Representative immunofluorescence images of DiI-LDL (red) uptake in KP4 cells or following expression of the indicated PCSK9 variants. Cells are co-stained for LAMP2 (green) and DAPI (blue). Scale bar: 10 μ m. **b.** Quantification of DiI-LDL fluorescence intensity from each condition depicted in a. (n = 10 fields/condition). Statistical significance was calculated using a one-way ANOVA with LSD correction. **c.** Representative immunofluorescence images of DiI-LDL (red) uptake in control HPAC cells (sgNT) or following knockout of PCSK9 (sgPCSK9). Scale bar: 10 μ m. **d.** Quantification of DiI-LDL fluorescence intensity from each condition depicted in c. Statistical significance was calculated using a one-way ANOVA with Bonferroni correction. (n = 10 fields/condition). **e.** Measurement of percentage confluence of HPAC cells transfected with sgNT or sgPCSK9. (n = 3 replicates per condition). **f.** Immunoblot of the indicated proteins in HPAC cells following ectopic expression of LDLR. **g.** Representative immunofluorescence images of DiI-LDL (red) uptake in control HPAC cells following ectopic expression of LDLR. Scale bar: 5 μ m. **h.** Quantification of DiI-LDL fluorescence intensity from each condition depicted in g. Control: n = 14 fields/condition, LDLR: n = 10 fields/condition. Statistical significance was calculated using a two-tailed t-test. **i.** Measurement of percentage confluence of control (eGFP) HPAC cells and following expression of LDLR. (n = 3 replicates per condition). **j.** Representative H&E images of tumor burden (red outline) in the liver 4 weeks post intra-splenic injection of HPAC cells with or without ectopic LDLR expression. Scale bars: 2 mm. **k.** Quantification of percent liver invasion from n = 5 mice/condition from data depicted in j. Statistical significance was calculated using a two-tailed t-test. **l.** Immunoblot of the indicated proteins in KPC3 cells (HY16936) following CRISPR mediated knockout of Pcsk9. **m.** Representative immunofluorescence images of DiI-LDL (red) uptake in control KPC3 cells (sgNT) or following knockout of Pcsk9 (sgPcsk9). Scale bar: 10 μ m. **n.** Quantification of DiI-LDL fluorescence intensity from each condition depicted in m. Statistical significance was calculated using a one-way ANOVA with Bonferroni correction. (n = 10 fields/condition). **o.** Heatmap showing expression levels of the indicated cholesterol biosynthesis genes measured by qRT-PCR and represented as z scores, following CRISPR mediated knockout of Pcsk9 in KPC3 cells. **p.** Measurement of percentage confluence of KPC3 cells transfected with sgNT or sgPcsk9. (n = 3 replicates per condition). **q.** Representative H&E images showing tumor burden (red outline) in the lungs (top) and liver (bottom) 2 weeks post tail-vein or intra-splenic injection, respectively, of KPC3 cells transfected with sgNT or sgPcsk9. Scale bars: 1 mm. **r,s.** Quantification of percentage tumor burden in the lung (r) and liver (s) from the experiment in q. Statistical significance was calculated using a one-way ANOVA with Bonferroni correction. (n = 5 mice/group). **t.** Image of tumors excised from the pancreas 2 weeks post orthotopic transplantation of KPC3 cells expressing sgNT or sgPcsk9. **u.** Quantification of tumor weight in each condition depicted in t. Statistical significance was calculated using a one-way ANOVA with Bonferroni correction. (n = 5 tumors/condition). All error bars represent standard deviation of the mean. For gel source data, see Supplementary Fig. 1.

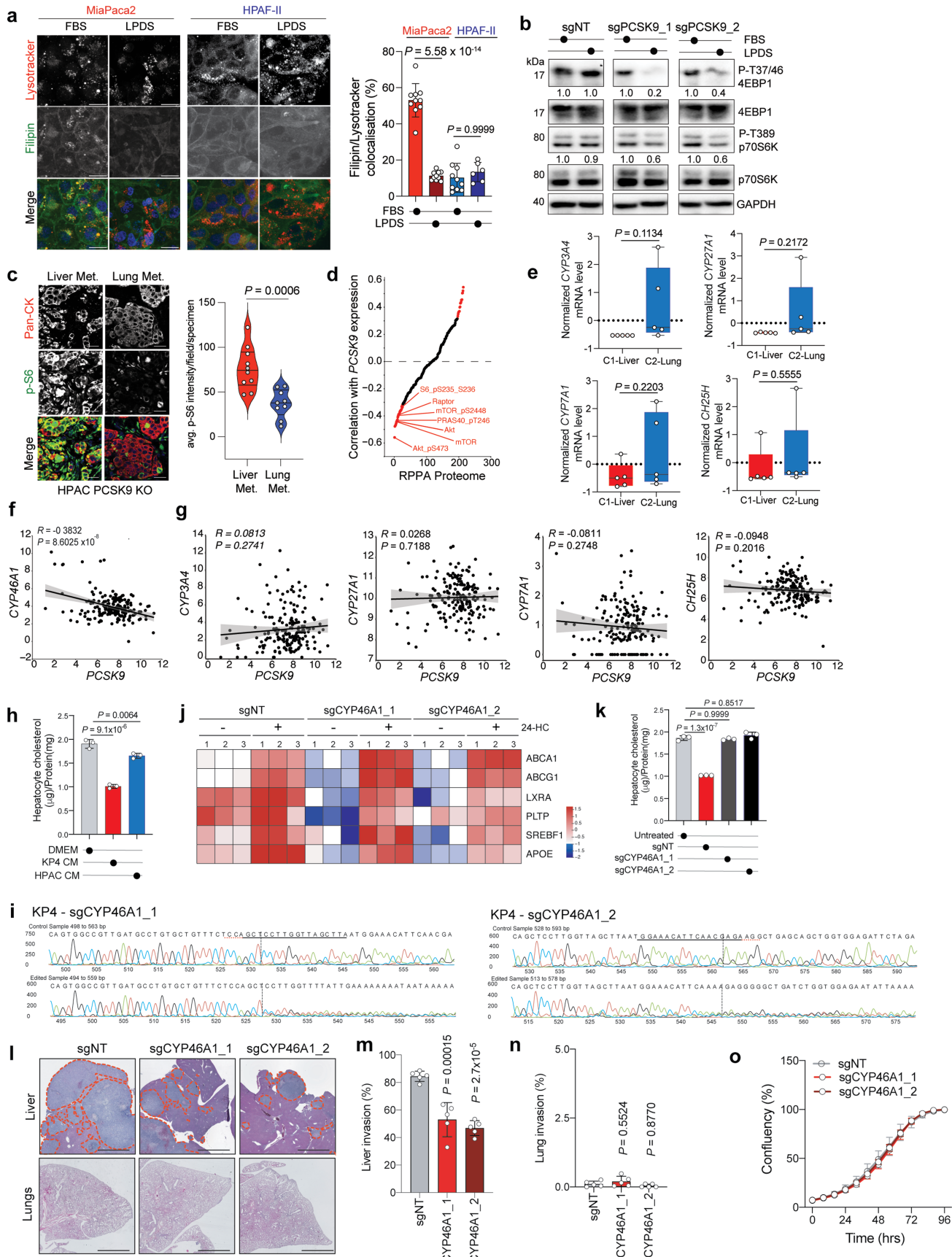


Extended Data Fig. 8 | PCSK9 expression level is organ dependent.

a. Representative immunofluorescence images depicting CK19 (red) and Pcsk9 (green) staining in mouse MT23 derived tumors 2 weeks post orthotopic transplant into the pancreas, intra-splenic injection to seed the liver and tail-vein injection to seed the lungs of C57Bl/6 mice. Scale bars: 50 μ m.

b. Quantification of Pcsk9 staining intensity in CK19 positive ductal structures from tumours grown in the pancreas ($n = 3$ mice; 12 fields), liver ($n = 3$ mice; 10 fields) and lung ($n = 3$ mice; 11 fields). Statistical significance was calculated using a one-way ANOVA with Bonferroni correction.

Article

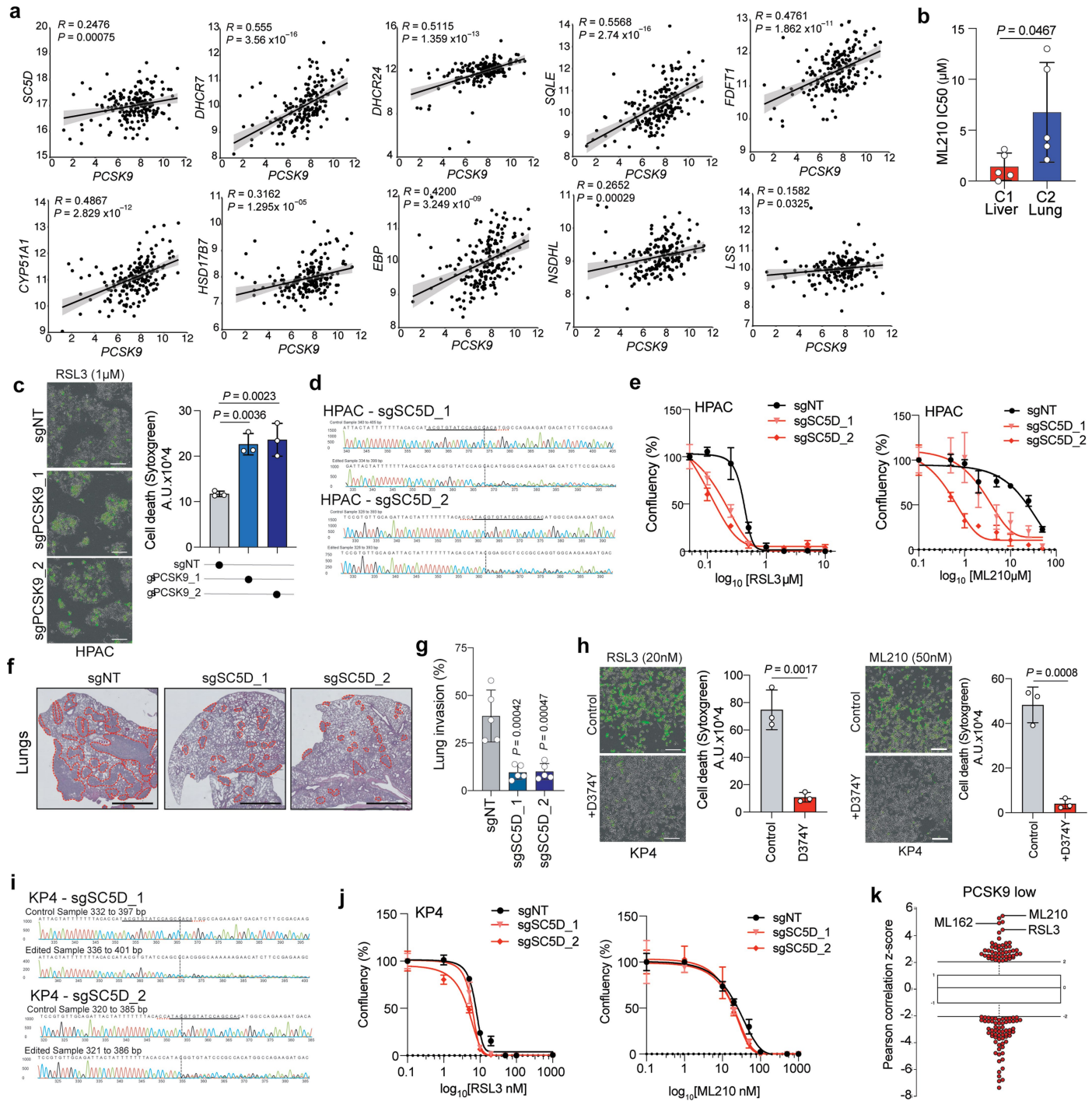


Extended Data Fig. 9 | See next page for caption.

Extended Data Fig. 9 | Liver-avid PDAC cells utilize cholesterol to activate mTORC1 and condition the liver microenvironment. **a.** Representative immunofluorescence images (left) and quantification (right) of Filatin staining in C1-Liver (MiaPaCa2) and C2-Lung (HPAF-II) cell lines growth in DMEM with FBS or LPDS for 72 h. Statistical significance was calculated using a one-way ANOVA followed by pairwise t-tests with Bonferroni correction. Error bars depict standard deviation. n = 10 fields for MiaPaCa2 (DMEM and LPDS) and HPAF-II (DMEM) and n = 6 fields for HPAF-II LPDS. **b.** Immunoblot showing 4EBP1 and P70S6K phosphorylation and total protein levels in HPAC PCSK9 KO cells treated with LPDS for 72 h. **c.** Representative immunofluorescence images of p-S6 (Ser240/244) in HPAC PCSK9 KO liver and lung tumors. Scale bar: 20 μ m. Graph at right shows quantification of p-S6 (Ser240/244) staining intensity in n = 10 PDAC liver metastases and n = 9 PDAC lung metastases. Each data point represents the average of at least 4 fields/sample. Statistical significance was calculated using a two tail T-test. **d.** Analysis of RPPA shows that mTOR and mTOR targets are anti-correlated with PCSK9 levels. **e.** Normalized mRNA expression measured by quantitative real-time PCR of the indicated transcripts in C1-Liver (n = 5) and C2-Lung (n = 5) lines. Dots represent the average of 3 biological replicates per cell line. Statistical significance was calculated using a two-tailed t-test. Line within the box plot represents the median. **f,g.** Scatter plots showing anti-correlation between PCSK9 and CYP46A1 (f) and no correlation with other cholesterol hydroxylases (g). Data derived from TCGA PAAD dataset. Linear regression followed by Pearson correlation. Error bars depict standard error of the mean. (n = 183 PDAC specimens). **h.** Total intracellular cholesterol in mouse hepatocytes following

treatment with KP4 or HPAC CM for 24 h, normalized to total cell number. (n = 3 biological replicates). Statistical significance was calculated using a one-way ANOVA with Bonferroni correction. Error bars depict standard deviation. **i.** Sequencing reads showing successful deletion of CYP46A1 using 2 independent sgRNAs in KP4 cells. **j.** Heatmap depicting the expression levels of LXR target genes in mouse hepatocytes as measured by qRT-PCR, following treatment for 24 h with CM isolated from KP4 parental and CYP46A1 knockout cells or treated with 24-hydroxycholesterol (24-HC; 25 μ M). Each row represents a specific gene. Each column represents a biological replicate per condition. Expression levels are expressed as z-scores, with positive z-scores indicating higher expression (red) and negative z-scores indicating lower expression (blue). **k.** Total intracellular cholesterol in mouse hepatocytes following treatment with CM isolated from KP4 parental or CYP46A1KO CM, normalized to cell number. Statistical significance was calculated using a one-way ANOVA with Bonferroni correction. Error bars depict standard deviation. (n = 3 biological replicates/group). **l.** Representative H&E images showing tumor burden in the liver (top) and lungs (bottom) following intra-splenic or tail-vein injection, respectively, of KP4 cells following CRISPR mediated knockout of CYP46A1. (n = 5 mice/group). Scale Bar: 500 μ m. **m,n.** Percentage tumour area in the liver (m) and lungs (n) from samples shown in l. Statistical significance was calculated using one-way ANOVA with Bonferroni correction. Error bars depict standard deviation. **o.** Measurement of KP4 growth rate in vitro following CYP46A1 knockout. Error bars depict standard deviation. (n = 3 replicates per group).

Article



Extended Data Fig. 10 | Lung-avid PDAC cells utilize cholesterol synthesis to generate sterols that protect against ferroptosis. **a.** Scatter plots showing TCGA PAAD derived expression correlation between PCSK9 and individual cholesterol biosynthesis pathway genes. Linear regression followed by Pearson correlation. Error bars depict standard error of the mean. ($n = 183$ PDAC specimens). **b.** Average ML210 IC50 measurement in C1-Liver ($n = 5$) and C2-Lung ($n = 5$) lines. Statistical significance was calculated using a two-tailed *t*-test. Error bars depict standard deviation. ($n = 5$ lines per condition). **c.** SYTOXgreen images (left) and quantification (right) of HPAC cell death (green fluorescence) following knock-out of PCSK9 and treatment with RSL3 for 24 h. Statistical significance was calculated using a one-way ANOVA with Bonferroni correction. Error bars depict standard deviation. ($n = 3$ biological replicates/group). **d.** Sequencing reads showing successful CRISPR mediated deletion of SCSD in HPAC cells. **e.** Measurement of HPAC cell growth following knockout of SC5D and treatment with increasing doses of RSL3 (left) and ML210 (right) for 96 h. Error bars depict standard error of the mean. ($n = 3$ biological replicates/group). **f.** Representative H&E images showing tumor growth (red outline) in the lungs 4 weeks post tail-vein injection of HPAC cells following CRISPR mediated knockout of SC5D. Scale bars: 1 mm. **g.** Quantification of percentage tumor burden from the experiment in f. Statistical significance is calculated using a one-way ANOVA with Bonferroni correction. Error bars depict standard deviation. ($n = 5$ mice/group). **h.** SYTOXgreen images and quantification of KP4 cell death (green fluorescence) following expression of a control vector or PCSK9^{D374Y} and treatment with RSL3 or ML210 for 24 h. Statistical significance was calculated using a two-tailed *t*-test. Error bars depict standard deviation. ($n = 3$ biological replicates/group). Scale bar: 200 μ m. **i.** Sequencing reads showing successful CRISPR mediated deletion of SC5D in KP4 cells. **j.** Measurement of KP4 cell growth following knockout of SC5D and treatment with increasing doses of RSL3 (left) or ML210 (right) for 96 h. Error bars depict standard error of the mean. ($n = 3$ biological replicates per group). **k.** Cancer Therapeutics Response Portal (CTRP) analysis of inhibitor sensitivity associated with PCSK9 low status across all cancers. ($n = 860$ cell lines). Inhibitors of GPX4 are indicated. Box represents mean with interquartile multiplier of 0.5.

the lungs 4 weeks post tail-vein injection of HPAC cells following CRISPR mediated knockout of SC5D. Scale bars: 1 mm. **g.** Quantification of percentage tumor burden from the experiment in f. Statistical significance is calculated using a one-way ANOVA with Bonferroni correction. Error bars depict standard deviation. ($n = 5$ mice/group). **h.** SYTOXgreen images and quantification of KP4 cell death (green fluorescence) following expression of a control vector or PCSK9^{D374Y} and treatment with RSL3 or ML210 for 24 h. Statistical significance was calculated using a two-tailed *t*-test. Error bars depict standard deviation. ($n = 3$ biological replicates/group). Scale bar: 200 μ m. **i.** Sequencing reads showing successful CRISPR mediated deletion of SC5D in KP4 cells. **j.** Measurement of KP4 cell growth following knockout of SC5D and treatment with increasing doses of RSL3 (left) or ML210 (right) for 96 h. Error bars depict standard error of the mean. ($n = 3$ biological replicates per group). **k.** Cancer Therapeutics Response Portal (CTRP) analysis of inhibitor sensitivity associated with PCSK9 low status across all cancers. ($n = 860$ cell lines). Inhibitors of GPX4 are indicated. Box represents mean with interquartile multiplier of 0.5.

Reporting Summary

Nature Portfolio wishes to improve the reproducibility of the work that we publish. This form provides structure for consistency and transparency in reporting. For further information on Nature Portfolio policies, see our [Editorial Policies](#) and the [Editorial Policy Checklist](#).

Please do not complete any field with "not applicable" or n/a. Refer to the help text for what text to use if an item is not relevant to your study. For final submission: please carefully check your responses for accuracy; you will not be able to make changes later.

Statistics

For all statistical analyses, confirm that the following items are present in the figure legend, table legend, main text, or Methods section.

n/a Confirmed

- The exact sample size (n) for each experimental group/condition, given as a discrete number and unit of measurement
- A statement on whether measurements were taken from distinct samples or whether the same sample was measured repeatedly
- The statistical test(s) used AND whether they are one- or two-sided
Only common tests should be described solely by name; describe more complex techniques in the Methods section.
- A description of all covariates tested
- A description of any assumptions or corrections, such as tests of normality and adjustment for multiple comparisons
- A full description of the statistical parameters including central tendency (e.g. means) or other basic estimates (e.g. regression coefficient) AND variation (e.g. standard deviation) or associated estimates of uncertainty (e.g. confidence intervals)
- For null hypothesis testing, the test statistic (e.g. F , t , r) with confidence intervals, effect sizes, degrees of freedom and P value noted
Give P values as exact values whenever suitable.
- For Bayesian analysis, information on the choice of priors and Markov chain Monte Carlo settings
- For hierarchical and complex designs, identification of the appropriate level for tests and full reporting of outcomes
- Estimates of effect sizes (e.g. Cohen's d , Pearson's r), indicating how they were calculated

Our web collection on [statistics for biologists](#) contains articles on many of the points above.

Software and code

Policy information about [availability of computer code](#)

Data collection Flow cytometry data were collected using FACS DIVA, IVIS images were collected using Living Image Software, qRT-PCR using Biorad,

Data analysis Flow cytometry data were analysed using Flowjo, Images were analysed using FIJI, stastistics were performed using PRISM or Rstudio, Lightsheet imaging was analysed using Imaris v10.0.0.

For manuscripts utilizing custom algorithms or software that are central to the research but not yet described in published literature, software must be made available to editors and reviewers. We strongly encourage code deposition in a community repository (e.g. GitHub). See the Nature Portfolio [guidelines for submitting code & software](#) for further information.

Data

Policy information about [availability of data](#)

All manuscripts must include a [data availability statement](#). This statement should provide the following information, where applicable:

- Accession codes, unique identifiers, or web links for publicly available datasets
- A description of any restrictions on data availability
- For clinical datasets or third party data, please ensure that the statement adheres to our [policy](#)

All source data were provided. Analysis of single cell RNA seq was from a published dataset. All other datasets used were from TCGA or DEPMAP

Research involving human participants, their data, or biological material

Policy information about studies with [human participants or human data](#). See also policy information about [sex, gender \(identity/presentation\), and sexual orientation](#) and [race, ethnicity and racism](#).

Reporting on sex and gender

All sex and gender were reported in supplemental tables, both male and female were used

Reporting on race, ethnicity, or other socially relevant groupings

All race and ethnicity were reported in supplemental tables

Population characteristics

Population characteristics are stated in supplemental tables. Covariate elements are described in supplemental data. Patients were not clinically matched for the liver vs lung metastasis and the PD versus WB however no differences were found when analysing co variates. Patient from the German study were clinically matched.

Recruitment

Recruitment was not performed

Ethics oversight

IRB protocol 18-25787 and 134-15,20-1085 and 284 were followed

Note that full information on the approval of the study protocol must also be provided in the manuscript.

Field-specific reporting

Please select the one below that is the best fit for your research. If you are not sure, read the appropriate sections before making your selection.

Life sciences

Behavioural & social sciences

Ecological, evolutionary & environmental sciences

Life sciences study design

All studies must disclose on these points even when the disclosure is negative.

Sample size

Previous studies in similar contexts have used comparable sample sizes to detect meaningful differences or associations. Additionally, we ensured that the sample size was sufficient to observe trends and perform statistical analyses

Data exclusions

No data or animals were excluded from analysis

Replication

Experiments were repeated multiple times with similar results as indicated in figure legends.

Randomization

Concerning mouse experiments randomization was not applicable, as our study primarily involved untreated mice. Since no interventions were administered, there were no treatment groups requiring randomization. Instead, all mice were maintained under the same standardized conditions to minimize variability, including controlled housing, diet, and environmental factors. Covariates were therefore not a concern in this context.

Blinding

Blinding was not performed in the mouse experiments as the study did not involve any treatment; mice were only injected with cell lines, making blinding unnecessary for the experimental procedure. However, for immunohistochemistry (IHC) quantification, the pathologist assessing the samples was blinded to group allocation. For all other experiments, blinding was not conducted

Reporting for specific materials, systems and methods

We require information from authors about some types of materials, experimental systems and methods used in many studies. Here, indicate whether each material, system or method listed is relevant to your study. If you are not sure if a list item applies to your research, read the appropriate section before selecting a response.

Materials & experimental systems

- | | |
|-------------------------------------|---|
| n/a | Involved in the study |
| <input type="checkbox"/> | <input checked="" type="checkbox"/> Antibodies |
| <input type="checkbox"/> | <input checked="" type="checkbox"/> Eukaryotic cell lines |
| <input checked="" type="checkbox"/> | <input type="checkbox"/> Palaeontology and archaeology |
| <input type="checkbox"/> | <input checked="" type="checkbox"/> Animals and other organisms |
| <input checked="" type="checkbox"/> | <input type="checkbox"/> Clinical data |
| <input checked="" type="checkbox"/> | <input type="checkbox"/> Dual use research of concern |
| <input checked="" type="checkbox"/> | <input type="checkbox"/> Plants |

Methods

- | | |
|-------------------------------------|--|
| n/a | Involved in the study |
| <input checked="" type="checkbox"/> | <input type="checkbox"/> ChIP-seq |
| <input type="checkbox"/> | <input checked="" type="checkbox"/> Flow cytometry |
| <input checked="" type="checkbox"/> | <input type="checkbox"/> MRI-based neuroimaging |

Antibodies

Antibodies used	PCSK9 (Catalog #85813, Cell Signaling), LDLR (Catalog #10785-1-AP, Proteintech), E-cadherin (Catalog #14472S, Cell Signaling), ZEB1 (Catalog #3396S, Cell Signaling), GAPDH (Catalog #SC-32233, Santa Cruz), HMGCR (Catalog #Ab242315, Abcam), SQLE (Catalog #12544-1-AP, Proteintech), FDFT1 (Catalog #13128-1-AP, Proteintech), LAMP2 (Catalog #sc-18822, Santa Cruz), CK19 (Catalog #Ab2133570, DSHB), LAMP1 (Catalog #1D4B, DSHB), LDLR (Catalog #ab275614, Abcam), Pancytokeratin (Catalog #LS-B16812-50, LS Bio), Abca1 (Catalog #ab18180, Abcam), GATA6 (Catalog #5851, Cell Signaling), ZEB1 (Catalog #HPA027524, Sigma), FSP1 (Catalog #20886-1-AP, Proteintech), GPX4 (Catalog #ab125066, Proteintech), NRF2 (Catalog #12721, Cell Signaling), SLC7A11 (Catalog #26864-1-AP, Proteintech), P-SMAD2/3 (Catalog #8828, Cell Signaling), SMAD2/3 (Catalog #3102, Cell Signaling), SREPB2 (Catalog #ab30682, Abcam), Vinculin (Catalog #V9131, Sigma), GFP Antibody (Catalog #A-31852, Thermo Fisher), Alpha Smooth Actin (Catalog #F3777, Sigma), mCherry (Catalog #74003TP594, Thermo Fisher), 4EBP1 (Catalog #9644S, Cell Signaling), P4EBP1 THR37/46 (Catalog #2855, Cell Signaling), P70S6K (Catalog #9202S, Cell Signaling), P-P70S6K T389 (Catalog #9234S, Cell Signaling), P-S6 (240/244) (Catalog #5364, Cell Signaling), Anti-Rabbit IgG (Catalog #PI-1000, Vector Lab), Anti-Mouse IgG (Catalog #PI-2000, Vector Lab), Anti-Rabbit (Catalog #PI-1000, Vector Lab), Alexa Fluor 488 (Catalog #A11029, Invitrogen), Alexa Fluor 555 (Catalog #A21429, Invitrogen), Alexa Fluor 555 (Catalog #A21422, Invitrogen), Alexa Fluor 555 (Catalog #A21434, Invitrogen), and Alexa Fluor 647 (Catalog #A21450, Invitrogen).
Validation	All primary antibodies used in this study were validated for the respective species and applications as outlined by the manufacturers. The antibodies were selected based on their specificity and proven performance in various applications, including Western blotting, immunohistochemistry, and immunofluorescence. Specific validation statements from the manufacturers regarding each antibody's use in the intended species and applications were considered, and relevant information can be found on the manufacturers' websites.

Eukaryotic cell lines

Policy information about [cell lines and Sex and Gender in Research](#)

Cell line source(s)	MiaPaCa-2, KP4, PaTu8988T, PSN1, Panc-1, YAPC, PaTu8902, CAPAN-2, HPAC, HPAF-II and HEK-293T were obtained from the American Type Culture Collection (ATCC) or DSMZ. MT23 and MM10 cells were established from Pdx1-cre+; KrasLSL-G12D+/; Trp53R172H/+ mice, backcrossed into a C57BL/6 background, and isolated from the pancreas and liver, respectively (provided by Dr. Chang-il Hwang, University of California, Davis). FC1245 (KPC1) were provided by Dr. David Tuveson (CSHL); HY15549 (KPC2) and HY16936 (KPC3) were provided by Dr. Ronald DePinho (MD Anderson); MT3 (KPC4) were provided by Dr. Chang-il Hwang and Dr. David Tuveson and were all derived from Pdx1-cre+; KrasLSL-G12D+/; Trp53 R172H/+ mice.
Authentication	All human cell lines acquired from ATCC and DSMZ were validated by fingerprinting visual inspection and careful maintenance
Mycoplasma contamination	Routing testing for mycoplasma was conducted by PCR. All cell lines tested negative for mycoplasma
Commonly misidentified lines (See ICLAC register)	No commonly misidentified cell lines were used in this study

Animals and other research organisms

Policy information about [studies involving animals; ARRIVE guidelines](#) recommended for reporting animal research, and [Sex and Gender in Research](#)

Laboratory animals	6-8 weeks C57BL/6 and 6-8 weeks NOD.CG-Prkdcscid Il2rgtm1Wjl/Szj (NSG) were purchased from Jackson laboratories
Wild animals	No wild animals were used in this study
Reporting on sex	Both male and female mice were used
Field-collected samples	No field collected samples were used in this study
Ethics oversight	All experiments involving laboratory animals were approved

Note that full information on the approval of the study protocol must also be provided in the manuscript.

Plants

Seed stocks	N/A
Novel plant genotypes	N/A
Authentication	N/A

Flow Cytometry

Plots

Confirm that:

- The axis labels state the marker and fluorochrome used (e.g. CD4-FITC).
- The axis scales are clearly visible. Include numbers along axes only for bottom left plot of group (a 'group' is an analysis of identical markers).
- All plots are contour plots with outliers or pseudocolor plots.
- A numerical value for number of cells or percentage (with statistics) is provided.

Methodology

Sample preparation	For surface LDL staining of human cell lines, cells were stained with APC-LDLR, For Dil-LDL cells were stained with Dil-LDL.
Instrument	Cells were analysed on a BD LSR Fortessa and analysed by FlowJo Software (FlowJo V10)
Software	FACS DIVA was used to collect the data which were analysed using FlowJo V10
Cell population abundance	The purity of cells was confirmed by analyses and was usually >90%
Gating strategy	Appropriate gating strategies were applied to exclude debris and ensure accurate analysis of single cells. Data were expressed as mean fluorescence intensity (MFI)

- Tick this box to confirm that a figure exemplifying the gating strategy is provided in the Supplementary Information.

